Improving River Flood Extent Delineation From Synthetic Aperture Radar Using Airborne Laser Altimetry

Article

Published Version

Improving River Flood Extent Delineation From Synthetic Aperture Radar Using Airborne Laser Altimetry

David C. Mason, Matthew S. Horritt, Johanna T. Dall'Amico, Tania R. Scott, and Paul D. Bates

Abstract—**Flood extent maps that are derived from synthetic aperture radar (SAR) images provide spatially distributed data for validating hydraulic models of river flood flow. The accuracy of such maps is reduced by a number of factors, including variation in backscatter from the different land cover types that are adjacent to the flood, changes in returns from the water surface that are caused by different meteorological conditions, and the presence of emergent vegetation. This paper describes how improved accuracy can be achieved by modifying an existing flood extent delineation algorithm to use airborne laser altimetry [light detection and ranging (lidar)] as well as SAR data. The lidar data provide an additional constraint that waterline heights should vary smoothly along the flooded reach. The method was tested on a SAR image of a flood for which contemporaneous aerial photography existed, together with lidar data of the unflooded reach. The waterline heights of the SAR flood extent that was conditioned on both SAR and lidar data matched the corresponding heights from the aerial photograph waterline significantly more closely than those from the SAR flood extent that was conditioned only on SAR data. For waterline heights in areas of low slope and vegetation, the root-mean-square error on the height differences reduced from 221.1 cm for the latter case to 55.5 cm for the former.**

Index Terms—**Data fusion, hydrology, lidar, snake.**

I. INTRODUCTION

FLOOD extent maps that are derived from remotely sensed data are of considerable use in hydrology, providing spatially distributed data for validation of hydraulic models of river flood flow, for emergency flood relief management, and for development of spatially accurate hazard maps [1], [2]. The all-weather day–night capability of synthetic aperture radar (SAR) sensors gives these a considerable advantage for flood mapping over sensors operating at visible or infrared wavelengths, as the latter ones are unable to penetrate the cloud that often accompanies flood events. This advantage is tempered by the fact that a number of factors conspire to reduce the accuracy of flood maps that are derived from SAR imagery. These include the substantial variation in backscatter from the different land cover types that are adjacent to the flood, the changes in returns from the water surface that are caused by different meteorological conditions, the presence of emergent vegetation, and the effects of man-made structures in urban areas. This paper describes a study to reduce inaccuracies from some of these sources in an existing flood extent delineation algorithm by using an additional data source, namely, airborne laser altimetry.

The simplest model of SAR backscatter from a river flood assumes that the water surface is smoother than the surrounding land and acts as a specular reflector, reflecting radiation away from a side-looking sensor, so that the water appears dark compared to the land. Two factors complicating the simple specular reflection model in practice are the effects of wind or rain roughening of the water surface, and emergent vegetation. The relationship between SAR backscatter and surface roughness that is caused by wind blowing over the oceans is well understood [3], and the effect may raise the backscatter from the water to similar or greater levels than the adjacent land [4], [5]. Wind roughening of a river flood surface can give rise to similar effects, but these can have substantial spatial variation, depending on the local topography, which determines the fetch for a given wind direction. The presence of emergent vegetation can give rise to multiple reflections between the water and the vegetation, leading to a substantial enhancement of backscatter, the magnitude of which is a function of radar wavelength, look angle, and polarization. The effect has been observed in a number of studies of flooded forest and marshland (e.g., [6]–[9]), and the increase in backscatter has been modeled mathematically in [10]. Enhanced backscatter from the water surface that is caused by wind roughening or emergent vegetation will also result in an increased level of noise due to the multiplicative nature of noise in SAR images.

A number of methods for the automated delineation of flood extent in SAR imagery of both fluvial and tidal environments have been developed [4], [5], [9], [11]–[21]. Several of these studies have illustrated the great potential of SAR sensors for synoptic observation of large flooding events. An automatic technique for delineating a fluvial flood using a statistical active contour model (or snake) that is applied to a SAR image to identify areas of homogeneous speckle statistics is described in [18] and [19]. This assumes that single-frequency single-polarization SAR intensities are available and was aimed at producing an observed flood extent against which to validate

a modeled flood extent. Due to the difficulties of imaging urban areas using SAR, its use is limited to large-area mapping of floods in rural areas. The SAR segmentation uses both local tone and texture measures, and is capable of accurate feature boundary representation. The method was applied to a flood that was imaged using the ERS-1 satellite SAR sensor and proven to be capable of identifying 75% of the flooded area correctly, with 70% of the waterline coinciding with ground data within 20 m. The main error in waterline position was found to be due to unflooded short vegetation that was adjacent to the flood giving similar radar returns to open water, causing an overestimation of flood extent. The loss of flood extent due to emergent vegetation was found to be a secondary source of error.

Further work on this topic [22], [23] found that, as a result of these error sources and the relatively large size of the European Remote Sensing Satellite (ERS) SAR pixel, the heights of the SAR waterline along a flooded reach could sometimes be in error by several meters (although, generally, it was much less) and could exhibit significant noise. One reason for this was that there was no constraint that the waterline heights should vary smoothly along the reach, whereas, in reality, the longitudinal slope of typical flood flows is low $(\sim 0.001 - 0.0001 \text{ m} \cdot \text{m}^{-1})$, and changes in slope are very gradual. With this level of differences, the SAR image becomes much less useful for model flood extent validation than it could otherwise be.

Horritt *et al.* [19] point out that their flood extent mapping procedure identifying the flood as a region of relatively homogeneous speckle statistics may be improved by the adoption of a model-based approach. In this vein, this paper describes the use of light detection and ranging (lidar) data to modify the SAR waterline, so that it becomes more useful for validation. The snake algorithm [18], [19] is modified to look not only at SAR image space but also at lidar digital terrain model (DTM) and vegetation height maps, so that the snake can be conditioned to be smoothly varying in ground height as well as in SAR intensities and textures. This should reduce errors that are caused by unflooded vegetation that is adjacent to the flood giving similar returns to open water and also errors due to the SAR pixel size. It could also help somewhat in reducing errors due to emergent vegetation. An additional benefit of producing a more smoothly varying waterline is that it may allow the development of improved performance measures for flood extent validation based on patterns of height differences rather than on patterns of wet or dry pixels, as currently done [24]. The algorithm specifically sets out to improve the vertical accuracy of the SAR waterline, although any improvement should also lead to improvement in the horizontal waterline accuracy due to their correlations that are contained within the DTM.

Used in this way, the lidar data may actually play a dual role in the modeling process, as lidar is often used to parameterize the hydraulic model being validated, with the lidar DTM providing the model bathymetry and possibly the vegetation heights being used to estimate bottom friction [22]. However, the use of lidar data in SAR waterline extraction as well as model parameterization does not undermine the independence of the SAR waterline in the validation process.
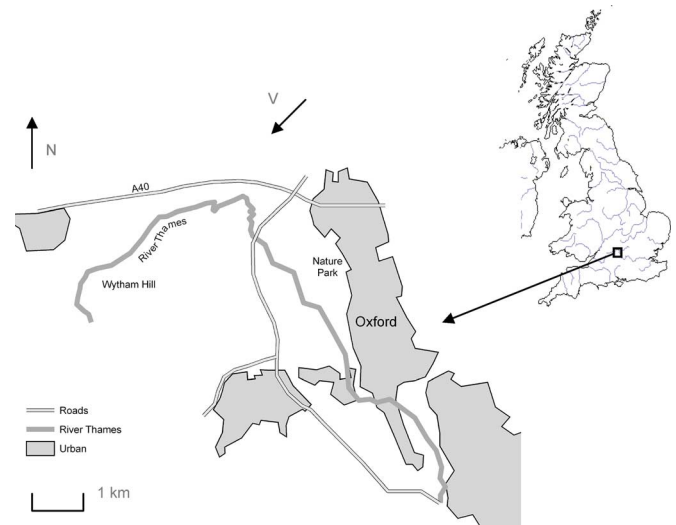

Fig. 1. Location of the test area.

II. TEST DATA SET

An ideal data set on which to validate the method would be from a flood for which both satellite SAR data and simultaneous aerial photography were available, so that the SAR snake waterlines that are conditioned without and with the lidar data could be compared with the waterline from the aerial photographs. In addition, lidar data of the unflooded area should be available.

Biggin and Blyth [25] acquired oblique aerial photos of a flood on the Thames west of Oxford, U.K., on December 4, 1992, at the same time (to within 2 h) as an ERS-1 SAR overpass of the area. The Thames is a low-relief slow-response catchment, and at this point along its course, the river discharge during a flood changes only very gradually, so that such timing differences are unimportant. The peak discharge for this event was measured at 76 m$^3 \cdot$ s^{-1}, which represents a $\sim$1-in-5-year-recurrence interval flow. The ERS-1 SAR image was acquired approximately 36 h after the flood peak when the discharge had dropped to 73 m$^3 \cdot$ s^{-1}, indicating the very slow response of the catchment. At the time of overpass, there was no wind or rain in the area. The location of the test area is shown in Fig. 1, and an example of the aerial photography is shown in Fig. 2. The floodplain over this reach is semirural, with the majority of fields being used at the time for pasture or having been ploughed. There are also several urban areas, and the region is crossed by a number of major roads and railways. The flood waterline was delineated by eye from the aerial photos and vectorized [19]. The waterline vectors were then georeferenced using an orthographic transform that is parameterized by a least squares method using 15–20 control points for each photograph. The error in the waterline position was assessed from waterline segments where the waterline was observed to lie alongside a hedgerow or field boundary that could be located on a 1 : 25 000 scale map and was found to be less than 20 m.

Fig. 2.   Example of the aerial photography in the upper section of the reach, looking southwest from the north of the region (the view direction is V in Fig. 1).

Lidar data at 1-m resolution were acquired for a section of this reach west of Oxford and approximately 12 km long by the Environment Agency of England and Wales (EA). The lidar was an Optech ALTM 2033 that was flown on a Cessna aircraft at 120 kn at a flying height of 900 m, with a laser firing rate of 33 kHz, a scanning frequency of 30 Hz, and a scanner half angle of 18°. The lidar heights were validated by the EA by comparing them with a set of global positioning system (GPS) heights of several flat unvegetated surfaces in the area. Based on a sample of 299 GPS readings, the lidar heights were found to have an rms error of 10.6 cm, which comprised a random error of 10.2 cm and a systematic error of 2.6 cm. Lidar height accuracy reduces on steeper slopes and in vegetated regions [26]. Lidar positional accuracy was about 0.4 m [27]. The postprocessed lidar DTM and vegetation height mask were obtained from the EA. These were degraded to 2-m pixel size to avoid too large a mismatch with the SAR pixel size of 12.5 m. Fig. 3 shows the lidar DTM with the high land of Wytham Hill in the west and the raised Oxford Nature Park in the east (see Fig. 1), both of which are relevant to this study. Fig. 3 also shows the aerial photo waterline overlain on the lidar DTM, with the waterline color representing its difference in height from the local mean waterline height (within 0.5-km distance). The presence of large sections of waterline having small differences (blue color) from the local mean height indicates that the aerial waterline height varies smoothly along the reach. The waterline includes instances of islands of higher ground that are surrounded by water. It is assumed here that all areas of water have been accurately mapped, so that the validation data are essentially error free.

III. Flood Extent Extraction From SAR Data

A. Algorithm Description

A detailed description of the algorithm to delineate a flood using an active contour model is given in [18], and only an overview is presented here. Active contour models or snakes are useful for converting incomplete or noisy edge maps into smooth continuous vector boundaries [5], [28]. The edge image space is searched using a dynamic curvilinear contour that is driven to be attracted to edge pixels using an energy minimization function, so that the contour can link together unconnected edge segments. The contour (snake) is represented in a piecewise linear fashion as a set of nodes (i.e., the coordinates of the snake points) that are linked by straight-line segments. Ivins and Porrill [29] developed a statistical snake that operates on the image itself rather than an edge image, dispensing with the need for a prior edge detection stage. Their technique involves estimating the local image mean intensity (tone) at a node using the pixels between this node and its adjacent nodes. This gives the advantage that noise due to SAR speckle is reduced by averaging pixel intensities along an edge while, at the same time, maintaining resolution that is perpendicular to the edge, giving accurate edge positioning. The local intensity variance (texture) is also calculated from these pixels, as this has proven to be a useful discriminator between different natural land-cover types having similar mean intensities in SAR imagery.

The statistical snake is formulated as an energy minimization problem with the total snake energy $E(\boldsymbol{u}(s))$ given by

$$E\left(\boldsymbol{u}(s)\right) = E_{\text{tension}} + E_{\text{curvature}} - \iint G\left(I(x,y)\right) dx\, dy \quad (1)$$
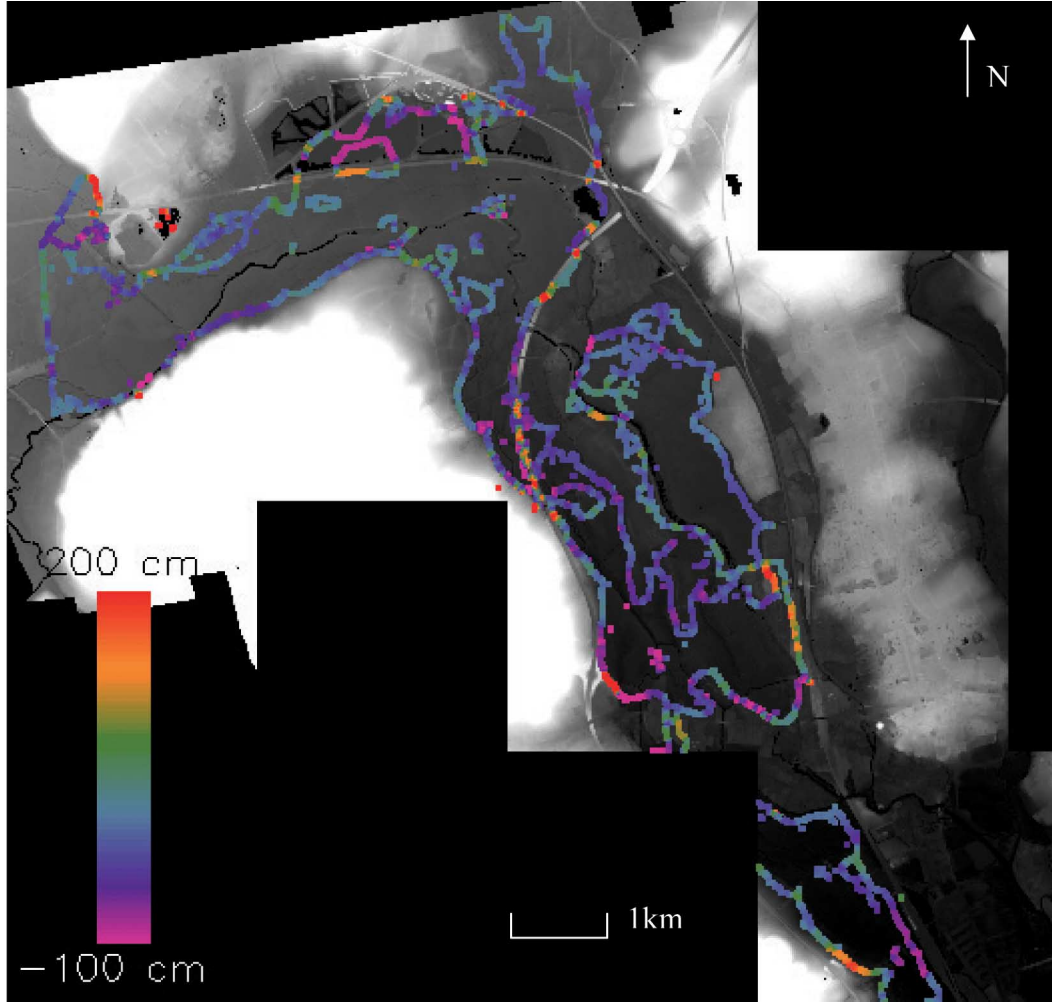
4/C   Fig. 3.   Aerial photo waterline overlain on the lidar DTM. The colors represent the difference in height of the waterline from the local mean waterline height.

238 where $\boldsymbol{u}(s) = (x(s), y(s))$ describes the contour position (x, y)
239 in the 2-D image space as a vector function of arc length
240 parameter s. E_{tension} and $E_{\text{curvature}}$ are energies that are gen-
241 erated by the model's internal tension and stiffness constraints,
242 which favor a smooth uncrenellated contour that is made up
243 of evenly spaced nodes (see the following). G is a goodness
244 function that assesses how well a set of image pixels $I(x, y)$
245 meets certain criteria. The total energy is minimized if the con-
246 tour encloses a region of pixels that is homogeneous in tone and
247 texture.
248   If the mean and variance of the intensities of the set of pixels
249 that are immediately at either side of a particular snake node are
250 measured, the knowledge of how these variables are distributed
251 can be used to estimate the probability that these pixels match
252 those that are already within the region that is enclosed by the
253 contour. Horritt [18] relates G to the log of this probability, with
254 the dependence on the measured sample mean μ', for example,
255 having the form

$$G(\mu') = 1 - n(\mu' - \mu)^2 / v k^2 \qquad (2)$$

256 where μ and v are the mean and variance of the seed population
257 that is already enclosed within the contour, respectively; n is

the sample size; and k is a parameter that can be adjusted 258
to tune algorithm performance. G is then equal to 1 for a 259
set of pixels with the expected mean but falls to zero if the 260
mean differs by $k\sqrt{(v/n)}$ (i.e., k standard deviations) from 261
the expected value. The parameter k is usually set at about 262
2 or 3 but may be increased further to allow for a level of 263
statistical inhomogeneity in the region being segmented. The 264
overall goodness function (with components that are based on 265
both the measured mean and variance) is limited to a minimum 266
value of -1.   267
    The roles of the tension and curvature constraints are to pro- 268
duce a contour of appropriate smoothness with evenly spaced 269
nodes, by a consideration of the balance between image and 270
curvature forces. Consider the situation that is shown in Fig. 4 271
for snake nodes at $\boldsymbol{u}_{i-1}$, $\boldsymbol{u}_i$, and $\boldsymbol{u}_{i+1}$ that are linked by unit 272
vectors $\boldsymbol{v}_i$ and $\boldsymbol{v}_{i+1}$. The local curvature is $\Delta\theta/\Delta s$, where $\Delta\theta$ 273
is the change of angle along arc length Δs. Horritt [18] gives 274
the contribution to the total curvature energy as   275

$$\Delta E_{\text{curvature}} = \gamma(\Delta\theta/\Delta s)^2/\Delta s = \gamma|\boldsymbol{v}_{i+1} - \boldsymbol{v}_i|^2/a_i \quad (3)$$

where a_i is the distance between the midpoints of $\boldsymbol{v}_i$ and $\boldsymbol{v}_{i+1}$, 276
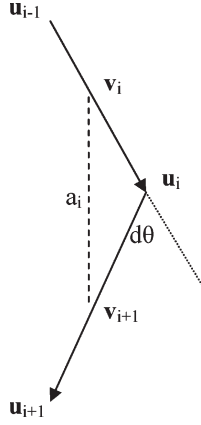and γ is a curvature energy weighting parameter. Equation (3) 277

Fig. 4.   Vectors for describing curvature and tension energies (after [18]).

278 is valid for small values of $\Delta\theta$. Similarly, the contribution to
279 the tension energy is given by

$$\Delta E_{\text{tension}} = \lambda \left(|\boldsymbol{u}_{i+1} - \boldsymbol{u}_i|^2 + |\boldsymbol{u}_i - \boldsymbol{u}_{i-1}|^2 \right) \qquad (4)$$

280 where λ is the tension energy weighting parameter. The mag-
281 nitudes of these energies can be adjusted using the weighting
282 parameters. Too large a value for the curvature parameter
283 will make the curvature term dominate the model energy and
284 produce an unrealistically smooth contour. Too large a value of
285 the tension parameter will favor a short contour and stifle the
286 growth of the snake.

287   The scheme that was used to minimize the energy is the
288 algorithm of Williams and Shah [28]. For each node at each
289 iteration, the change in energy dE is computed for moves to all
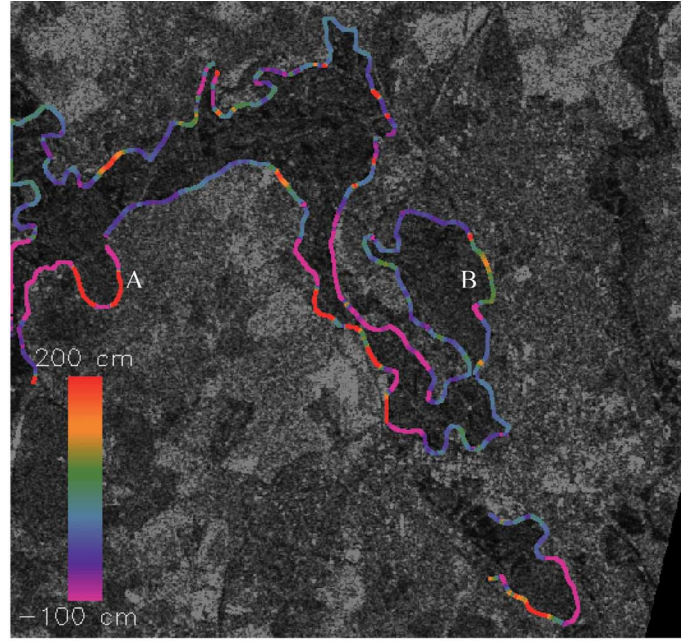290 eight neighbors of the node

$$dE = -GdA + dE_{\text{tension}} + dE_{\text{curvature}}. \qquad (5)$$

291   The lowest (most negative) dE is chosen. Obviously, dE is
292 equal to zero for no node movement. G is calculated along the
293 line segments linking the node with its two neighbors, and dA is
294 the local change in area. If G is positive, the snake is in a region
295 of homogeneous pixels, a positive dA is favored, and the snake
296 expands. If G is negative, the snake is in an inhomogeneous re-
297 gion, a negative dA is favored, and the snake retreats. The mean
298 and standard deviation of the seed population are calculated
299 from all pixels lying inside the contour every ten iterations.

300   The flooded region may not be simply connected, as islands
301 and isolated water bodies may form holes and outliers. To cope
302 with this, the algorithm incorporates a method for dealing with
303 complex topology and snake self-intersection. As an example,
304 a snake may spawn a smaller subsnake within itself to represent
305 an island.

B. *Implementation and Qualitative Assessment of Results*

307   A personal computer (PC)-based implementation of the al-
308 gorithm (Psnake NT) was used in this paper [30]. Psnake NT
309 is a software package that is available to the hydrological
310 modeling community for the semiautomatic extraction of flood

(a)

(b)

Fig. 5.   Waterline conditioned only on SAR data overlain on SAR data (a) for **4/C** parameter $k = 3$ and (b) $k = 2$. The colors represent the difference in height of the waterline from the local mean waterline height.

extents from SAR data. Fig. 5 shows snake waterlines that are 311 generated using SAR data only, for the number of standard 312 deviations k of 3 and 2, overlain on SAR data. It has been found 313 by experiment that k is probably the most important parameter 314 controlling the snake [19]. Other parameter settings were a 315 minimum node spacing of 6 pixels, a maximum node spacing 316 of 12 pixels, curvature parameter γ of 68.3, tension parameter λ 317 of 0.1, a texture weight of 0.2, and iterations of 200. The snake 318 was seeded (i.e., initialized) manually as a narrow strip lying 319

Fig. 6. Example error that might be corrected using lidar.
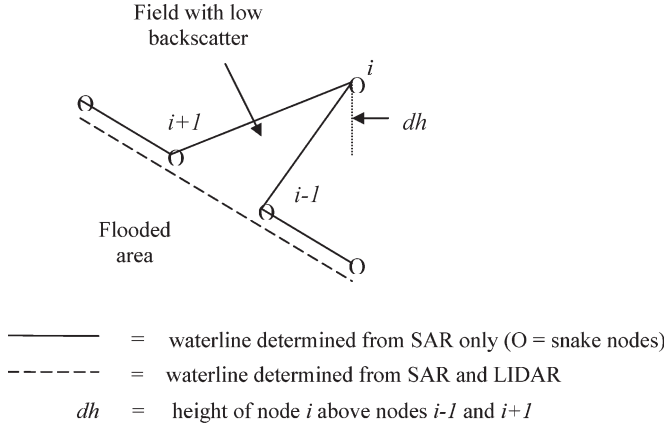
along the course of the unflooded river channel, ensuring that it contained only flooded pixels.

In Fig. 5, the snake shows a tendency to leak onto higher ground on Wytham Hill [point A in Fig. 5(a), see also Fig. 3]. This is likely to be due to the presence of vegetated fields, which correspond to areas of low SAR backscatter and are likely to be misclassified as flooded. While no ground reference data were acquired at the time of the flood, evidence for this comes from a recent aerial photograph that was obtained later than the SAR image. A further example of leakage of the snake onto higher ground is visible at point B in Fig. 5(a), where the snake has leaked onto the Oxford Nature Park, which is higher than the land toward the Thames yet again exhibits low SAR backscatter.

IV. FLOOD EXTENT EXTRACTION FROM SAR AND LIDAR DATA

A. Algorithm Modification

The snake algorithm was modified so that the snake was conditioned not only on the SAR image but also on the lidar DTM, so that it becomes smoothly varying in ground height as well as in SAR intensities and textures. The principle that was adopted was that the SAR image should still be the primary determinant of the flood extent. In most areas, the flood extent that was determined by the SAR will be correct within the SAR resolution, but where errors creep in the lidar can help to correct these.

The lidar DTM is able to provide a ground height at each pixel, so that each position $\boldsymbol{u}(x, y)$ becomes $\boldsymbol{u}(x, y, z)$. The modification involves using the lidar heights to measure curvatures and tensions at snake nodes in 3-D rather than 2-D space. Consider an instance where an unflooded field with low SAR backscatter is adjacent to a flood edge, such that the field is included in the SAR waterline determined by the snake (Fig. 6). As there will likely be a rise in height (dh) across the field that is perpendicular to the true flood edge, the error in the waterline will give rise to a significant component of curvature in the vertical plane, which will not be present in the waterline segments that are adjacent to the field. To be specific, in Psnake

NT, the contribution to the 3-D curvature energy at the snake node at $\boldsymbol{u}(x_i, y_i, z_i)$ from its two adjacent nodes is

$$\Delta E_{\text{curvature}} = \gamma |\boldsymbol{v}_{i+1} - \boldsymbol{v}_i|^2 / a_i = \left(c_{ix}^2 + c_{iy}^2 + c_{iz}^2\right) / a_i \quad (6)$$

where

$$c_{ix} = (x_{i+1} - x_i)/d_{i+1} - (x_i - x_{i-1})/d_i$$
$$c_{iy} = (y_{i+1} - y_i)/d_{i+1} - (y_i - y_{i-1})/d_i$$
$$c_{iz} = (z_{i+1} - z_i)/d_{i+1} - (z_i - z_{i-1})/d_i$$
$$d_i = \left((x_i - x_{i-1})^2 + (y_i - y_{i-1})^2 + (z_i - z_{i-1})^2\right)^{0.5}$$
$$d_{i+1} = \left((x_{i+1} - x_i)^2 + (y_{i+1} - y_i)^2 + (z_{i+1} - z_i)^2\right)^{0.5}$$
$$a_i = \Big(((x_{i+1} + x_i)/2 - (x_i + x_{i-1})/2)^2$$
$$+ ((y_{i+1} + y_i)/2 - (y_i + y_{i-1})/2)^2$$
$$+ ((z_{i+1} + z_i)/2 - (z_i + z_{i-1})/2)^2 \Big)^{0.5}$$

and the suffixes refer to the node numbers in Fig. 6. To reduce the vertical curvature component c_{iz}^2 at node i in Fig. 6, the snake will try to contract to drag node i back to be collinear with nodes $i - 1$ and $i + 1$, which will also reduce c_{ix}^2 and c_{iy}^2. The 3-D tension energy, which is proportional to $(d_{i+1}^2 + d_i^2)$, will also be reduced by this move.

A waterline error due to the presence of emergent vegetation at the edge of the flood might also have significant components of vertical curvature and tension that could be reduced by correcting the error. A complicating factor in this case is that the SAR and lidar forces might be acting against each other. In order to reduce the vertical curvature and tension by incorporating the area of enhanced backscatter into the flooded area, the inhomogeneity of the SAR returns in the flooded area would generally have to increase. Which force won out in a particular case would depend on their relative strengths. However, this effect is not the dominant source of error [19].

In order to take account of the fact that a change in height at a node should, in general, cause different changes in curvature and tension compared to the same magnitude change of node position in the xy plane, the lidar heights were scaled by weighting factor w_l with respect to the (x, y) coordinates.

The straightforward approach to combining the SAR and lidar data would be to use the existing algorithm with both data sets and simply calculate 3-D rather than 2-D curvature and tension energies. A possible objection to this might be that, if there were flooded mounds in the floodplain that are not visible to the SAR but visible to the lidar, these might retard the expansion of the snake and distort the eventual waterline. An alternative approach could be to use the algorithm with SAR data and 2-D curvatures and tensions only initially. Then, the snake iterations could continue using SAR and lidar data, and 3-D curvatures and tensions, causing the snake to adjust itself to correct errors where necessary. However, in cases where the waterline was significantly in error, it might be difficult to recover from these errors. For example, if the snake leaked onto higher ground, it might be impeded from returning to the true waterline position by a hollow in the higher ground. In practice, it turns out that the straightforward approach using

the existing algorithm and calculating 3-D curvatures and tensions works well enough.

The SAR data may have significantly lower resolution than the airborne lidar data, as in the present test data set comprising ERS satellite SAR data. In this case, it may be possible to correct the waterline position to sub-SAR pixel accuracy in a second pass of the algorithm. The idea would be to rescale the SAR image and the snake waterline from the first pass to the higher resolution of the lidar, and to continue iterating to try to move the snake nodes away from the centers of the enlarged SAR pixels to create a waterline varying more smoothly in height along its length. A constraint would be that a node should not be allowed to move outside its enlarged SAR pixel, as no further information could be extracted from the SAR image at this stage.

B. Implementation and Qualitative Assessment of Results

For the first pass of the modified algorithm, the lidar image was degraded to the same pixel size as the SAR image (12.5 m) by averaging the lidar heights within each SAR pixel. The parameter settings for this pass were the same as those for the snake that was conditioned on only the SAR data (other than for k and w_l). The initial value of lidar weight factor w_l was chosen by experiment to be 0.15. This took into account the fact that the leakage at Wytham Hill [at point A in Fig. 5(a)] occurs over a distance of about 0.5 km. Curvature at a node is calculated using the two adjacent nodes on either side of the central node, spanning four internode spacings. For an internode spacing of eight pixels, this corresponds to a distance of about 400 m, roughly matching that required. The w_l setting also reflected the facts that the lidar heights were expressed in millimeters and that a, for example, 1000-mm rise in the lidar height of the central node should give rise to a significant increase in 3-D curvature. Even though a node can only be moved horizontally by one SAR pixel at each iteration, this still amounts to a horizontal shift of 12.5 m, which is large compared to a 1-m vertical rise.

The original snake seed that was used contained only pixels south of the A40 road west of Oxford (Fig. 1), and it was found on the first pass that, with the 3-D curvature constraint, the snake would not expand into the flooded areas north of the embanked road, even though this was, on average, only 1.5 m higher than the fields surrounding it. In practice, floodwater from the Thames flows under the A40 onto the lower land to the north through culverts that are spaced at about 250-m intervals. To overcome this difficulty, additional snake seed pixels were inserted to the north of the A40, which were then able to expand into the northernmost part of the flooded region. The same snake seed was used for all snakes that were generated, whether they were conditioned using the lidar data or not.

The second pass took place at higher resolution, i.e., at the 2-m pixel spacing of the lidar data. The input to this pass was the snake output from the first pass, with the node coordinates scaled up by 6.25 to match the change in resolution. The SAR image was interpolated from 12.5 to 2 m using nearest neighbor interpolation. The number of iterations was set to 3,

(a)

(b)

Fig. 7. Waterline conditioned on SAR and lidar data overlain on SAR data (a) for parameter $k = 3$ and $w_l = 0.15$, and (b) for $k = 4$ and $w_l = 0.15$. The colors represent the difference in height of the waterline from the local mean waterline height. **4/C**

to ensure that the snake nodes would not move outside the SAR pixels within which they had stabilized after the first pass. The minimum and maximum node spacings were also upscaled to 37 and 74 pixels, respectively, ensuring similar 3-D curvatures to those on the first pass.

Fig. 7 shows snake waterlines that were conditioned on both SAR and lidar data, for k values of 3 and 4 and lidar weight $w_l = 0.15$, overlain on 12.5-m SAR data. It is clear that the tendency for the snake to leak to higher ground at Wytham Hill and at the Oxford Nature Park has been much reduced (see

also Fig. 3). A further benefit is that the snake appears to be more stable to parameter changes. For example, in Fig. 5, the snake that was conditioned only on SAR data shows substantial change when k is raised from 2 to 3, whereas in Fig. 7, the snake that was conditioned on SAR and lidar shows less change when k is raised from 3 to 4. This finding is born out more rigorously in the quantitative analysis described in the next section.

The main errors in waterline position that were corrected using the lidar data are due to the unflooded short vegetation that is adjacent to the flood giving similar returns to open water. The ability of the algorithm to correct loss of flood extent due to emergent vegetation is hardly tested using this data set, as this has few significant examples. The most obvious instances are emergent hedges between adjacent flooded fields, but these are generally of insufficient area to stop the snake subsuming them into its interior, even if conditioned only on SAR data.

V. PARAMETER OPTIMIZATION AND QUANTITATIVE COMPARISON OF METHODS

The snake parameters were optimized using a quantitative measurement of algorithm performance. The snake and aerial photo waterlines were first heighted by superimposing them on the lidar DTM. The snake waterline is defined only at the snake nodes. Only nodes on low slopes and in areas of short vegetation in the lidar vegetation height map were selected for heighting, as these are the ones that are likely to be heighted most accurately. The lower the slope, the smaller the node height error for a given error in its position. No requirements were made that selected nodes should have a strong SAR edge [indicated by a low G value (2)] associated with them, as this would reject nodes at the boundaries between the flood and an unflooded field giving low SAR backscatter, or between a region of emergent vegetation at the flood edge and an adjacent unflooded land (both giving high SAR backscatter).

For each snake node that was selected, the aerial photo height to associate with the snake height was found by finding the height of the closest aerial photograph waterline point. This was found by applying a distance-with-destination transform to the aerial photo waterline image. The distance-with-destination transform is a form of distance transform that stores, for each pixel in the transform image, its distance to the nearest waterline point and also the direction from which the minimum distance was propagated. This allows backtracking from a pixel to find its nearest waterline point [31]. Corroborating the finding of [19], the average separation distance was about 50 m, although this value was strongly influenced by a small number of pairs having large separations, and the average separation of 70% of the pairs having separations of less than 50 m was only 20 m. However, the pairs with large separation were not rejected, as they included examples where, e.g., the SAR waterline was displaced from the aerial photo waterline by a complete field width due to misclassification of the field as flooded. The anticipation was that these events would be less common when the snake was conditioned on the SAR and lidar data than on the SAR data alone.

Parameters were optimized by minimizing the sum of the squared height differences between the snake nodes and their corresponding aerial photo waterline points. To ensure that adjacent pairs of heights were largely uncorrelated, the pairs that were selected so far were thinned further, so that no pair was closer than 200 m to another. This distance was estimated by constructing a correlogram from the set of pairs [32] and was the distance at which the average correlation between adjacent pairs became less than 0.2. From the remaining pairs, the mean and standard deviations of the snake and aerial photograph waterline heights were calculated, as was the rms error of the height differences, with this being the variable to minimize in the parameter optimization. The mean height difference and the standard deviation of the differences were also calculated, and this allowed a paired t-test to be performed to test whether the differences were significantly nonzero. The paired t-test is used to exploit the fact that, while corresponding SAR and aerial photograph waterline heights will be correlated due to the gradual drop in height along the reach, the height differences at corresponding nodes will be uncorrelated due to the thinning process, as required by the paired test.

Only the most important parameters were investigated in the optimization procedure. For the snake that was conditioned on only SAR data, the parameter that was optimized was k. For the snake that was conditioned on SAR and lidar data, k and w_l were optimized.

Table I(a) shows the results of varying k for the snake that was conditioned on only the SAR data. The minimum rms error is 221.1 cm, which was obtained for $k = 2.0$. The associated high t value implies that there is a significant height difference at the 5% level between the snake and aerial photo waterlines. The corresponding snake is shown in Fig. 5(b). Higher values of k give significantly larger rms errors, and the high t values that were coupled with positive mean height differences imply that, for all these k values, the snake waterline heights are significantly higher than those of the aerial photograph.

Table I(b) shows the results of varying k for the snake that was conditioned on SAR and lidar data, with w_l held constant at 0.15. The minimum rms error is 55.5 cm, which was obtained for $k = 3.0$. The associated t value is not significantly nonzero, so that there is no significant difference between the snake and aerial photo waterline heights. The corresponding snake is shown in Fig. 7(a).

Table I(c) shows the results of varying w_l for the snake that was conditioned on SAR and lidar data, with k held constant at 3.0. The minimum rms error is obtained at $w_l = 0.15$. Over the ranges of k and w_l that were investigated, none of the t values are significantly nonzero, implying greater robustness to parameter changes than the case for the snake that was conditioned on only SAR data.

Table II gives the frequency tables of the absolute differences of the paired heights for the parameter sets giving the minimum rms errors for the snake that was conditioned on only the SAR data and the snake that was conditioned on SAR and lidar data. It can be seen that the increase in the rms error in the case of the snake that was conditioned only on SAR data is due almost entirely to the large number of pairs having height differences of greater than 300 cm. This is also apparent in Fig. 8, where the paired height differences for the two cases are plotted as a

TABLE I
RESULTS OF (a) VARYING k FOR THE SNAKE CONDITIONED ON ONLY THE
SAR DATA, (b) VARYING k FOR THE SNAKE CONDITIONED ON SAR AND
LIDAR DATA, WITH w_l HELD CONSTANT AT 0.15, AND (c) VARYING w_l
FOR THE SNAKE CONDITIONED ON SAR AND LIDAR DATA,
WITH k HELD CONSTANT AT 3.0

k	Number of height pairs	R.m.s. error in height (cm)	Mean height difference (cm)	t_0	Probability $t > \|t_0\|$ (one-sided test)	Relative height standard deviation (cm)
1.5	165	238.8	31.6	1.7	0.04	105.3
2.0	200	221.1	33.7	2.2	0.02	136.2
2.5	197	381.3	65.4	2.4	0.01	263.1
3.0	195	331.4	64.5	2.8	0.004	314.4
4.0	206	317.5	70.7	3.3	0.0005	379.1

(a)

k	Number of height pairs	R.m.s. error in height (cm)	Mean height difference (cm)	t_0	Probability $t > \|t_0\|$	Relative height standard deviation (cm)
2.8	195	57.8	-1.5	-0.4	0.35	43.5
3.0	191	55.5	-4.3	-1.0	0.15	42.6
3.2	190	86.6	-3.1	-0.5	0.30	52.6
3.5	195	120.8	5.2	0.6	0.28	65.4
4.0	195	63.7	4.5	1.0	0.15	48.9

(b)

w_l	Number of height pairs	R.m.s. error in height (cm)	Mean height difference (cm)	t_0	Probability $t > \|t_0\|$	Relative height standard deviation (cm)
0.10	187	90.2	-0.1	-0.1	0.46	47.4
0.14	196	61.0	5.4	1.2	0.10	43.0
0.15	191	55.5	-4.3	-1.0	0.15	42.6
0.16	191	55.8	0.7	0.2	0.42	43.5
0.20	195	81.5	-9.0	-1.5	0.07	54.7

(c)

TABLE II
FREQUENCY TABLES OF THE ABSOLUTE DIFFERENCES OF PAIRED
HEIGHTS FOR THE PARAMETER SETS GIVING THE MINIMUM RMS
ERRORS FOR THE SNAKE CONDITIONED ON ONLY THE SAR DATA
AND THE SNAKE CONDITIONED ON SAR AND LIDAR DATA

	0-49cm	50-99cm	100-149cm	150-199cm	200-249cm	250-299cm	300-499cm	>=500cm
Snake conditioned on SAR data ($k = 2.0$)	155	20	9	3	3	1	3	6
Snake conditioned on SAR and LiDAR data ($k = 3.0$, $w_l = 0.15$)	154	20	9	5	2	1	0	0

580 function of distance downstream. The main effect of the lidar
581 data is to correct errors in the sections of waterline containing
582 these outliers, when the snake is conditioned on both SAR and
583 lidar.

584 The effect of the second pass of the algorithm in correcting
585 the waterline position to sub-SAR pixel accuracy was also
586 assessed. For the parameter set giving the minimum rms error
587 for the snake that was conditioned on SAR and lidar data
588 ($k = 3.0$ and $w_l = 0.15$), the algorithm was run for only the
589 first pass. The minimum rms error was 58.1 cm, which is
590 only slightly higher than the 55.5 cm that was achieved when
591 both passes were employed. There was slightly more difference
592 when k was raised to 4.0 and when the rms error increased to
593 70.8 from 63.7. This indicates that the main reduction in error is
594 being generated in the first pass and that the second gives only
595 a second-order improvement. This may be partly because only
596 snake nodes on low slopes have been selected, and thus, height
597 differences across the SAR pixel, due to its size, will be small.

VI. DISCUSSION 598

The method may be applied to the validation of the flood 599
models of other river reaches, with the only prerequisites 600
additional to the usual data required to set up a hydraulic 601
model (e.g., an inflow hydrograph and river channel cross- 602
sectional data) being the availability of SAR imagery of the 603
river in flood and reasonably contemporaneous lidar data of 604
the unflooded reach. It would be relatively straightforward to 605
make the procedure operational. Lidar data are now often used 606
to parameterize the hydraulic model, making it more likely that 607
they would also be available to improve the SAR waterline. 608
It would be straightforward to implement the modified algo- 609
rithm within the Psnake NT software package. For this catch- 610
ment, the algorithm processing time was less than 1 min on a 611
Pentium IV personal computer. 612

The emphasis in the foregoing has been on ERS satellite 613
SAR data because of the availability of simultaneous ERS SAR 614
and aerial photography of the 1992 Oxford flood. While ERS 615
SAR data have poorer resolution than airborne lidar data, the 616
technique should also be applicable in cases where the SAR 617
resolution is similar to that of the lidar (e.g., airborne SAR), 618
in which case a second pass of the algorithm would certainly 619
be unnecessary. The algorithm of [18] and [19] has been used 620
to delineate flood extents in airborne SAR imagery [33], [34]. 621
However, given the increasing number of satellite SAR sensors 622
flying or planned and the difficulty of flying aircraft in poor 623
weather often accompanying floods, satellite SARs are likely 624
to remain to be a major source of SAR data for flood mapping 625
in the future. While the ERS SAR sensor has single VV polar- 626
ization and a fixed $23°$ viewing angle, the advent of later sensors 627
with higher resolutions, multiple polarizations, and variable 628
viewing angles (e.g., RADARSAT and Envisat Advanced SAR) 629
has allowed improved flood delineation (e.g., [15]). The high- 630
resolution satellite SAR sensors due for launch shortly (e.g., 631
RADARSAT-2, TerraSAR, and the Cosmo-Skymed constella- 632
tion) will have resolutions that match or almost match that of 633
airborne lidar. 634

Production of a more smoothly varying waterline may allow 635
the development of improved performance measures for flood 636
extent validation based on patterns of height differences be- 637
tween observed and modeled waterlines rather than on patterns 638
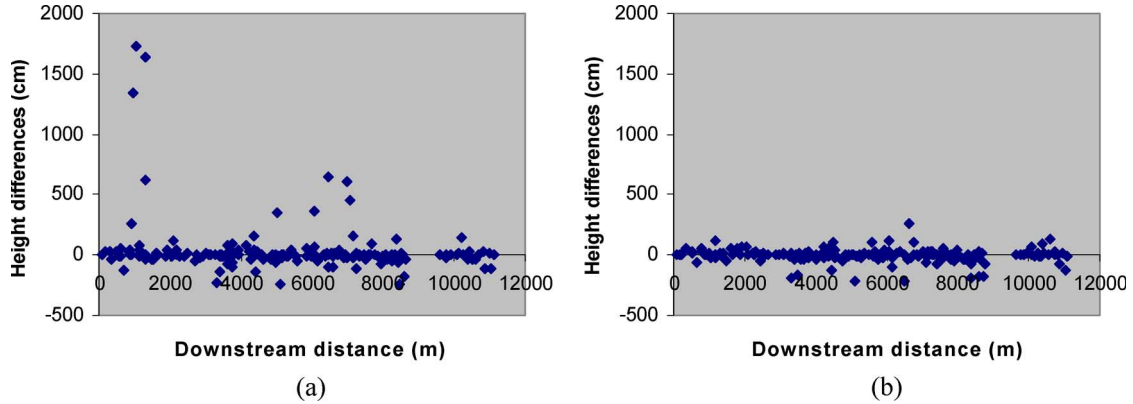of wet or dry pixels, as currently done. Aronica *et al.* [24] 639

Fig. 8.   Paired height differences versus distance downstream for the parameter sets giving the minimum rms errors for the snake that was conditioned on (a) SAR data and (b) SAR and lidar data.

640 describe current performance measures based on binary pat-
641 terns. One measure representative of these is

$$F^{(2)} = \left(A_{\text{obs}} \bigcap A_{\text{mod}}\right) / \left(A_{\text{obs}} \bigcup A_{\text{mod}}\right) \qquad (7)$$

642 where A_{obs} and A_{mod} represent the set of pixels that are ob-
643 served to be inundated and predicted as inundated, respectively.
644 $F^{(2)}$ is equal to 1 when observed and predicted areas coincide
645 exactly and equal to 0 when no overlap between predicted and
646 observed areas exists. A performance measure based on height
647 differences might have several advantages over one such as
648 $F^{(2)}$ based on binary pattern data. First, as the distribution of
649 t is known, it is possible to estimate the probability $P(t > |t_0|)$
650 of obtaining a t value that is greater than the absolute value
651 of that measured (t_0), whereas $F^{(2)}$ is simply a weight factor.
652 Second, the height difference measure between two model
653 runs with different parameter settings might turn out to be
654 more sensitive than $F^{(2)}$, because a small change in mean
655 height might cause a large change in $P(t > |t_0|)$ yet only a
656 small change in $F^{(2)}$. Third, the sign of the t value identifies
657 whether an overprediction or an underprediction has occurred,
658 whereas $F^{(2)}$ may give similar values for overprediction and
659 underprediction.
660   In this case, the parameters of the snake that was generated
661 using SAR and lidar have been optimized using the aerial
662 photo waterline, but this will not be available in the more usual
663 situation in which the snake is being used to validate a model
664 waterline. It is interesting that, for those nodes in areas of low
665 slope and low vegetation, the standard deviation of their heights
666 relative to their local mean height (within an 0.5-km distance)
667 is a minimum at the same parameter setting at which the rms
668 error of height differences between snake and aerial photo
669 waterlines is minimized [Table I(b) and (c)]. This presumably
670 reflects the fact that the snake is most smoothly varying when
671 the relative height standard deviation is minimized, and it may
672 be possible to use this measure as a surrogate for optimizing the
673 snake parameters when using the snake to validate a modeled
674 flood extent. However, a more likely scenario is that a single
675 optimum parameter set would not be sought in this situation. In
676 flood model validation, emphasis is now placed on associating
677 uncertainties with model flood extents, by deriving flood extent

678 probability maps showing the probability of each pixel being
679 flooded, given a flood event of the given magnitude. It has
680 been found that, for a particular event, many different sets
681 of model parameters may give flood extents that match the
682 observed extent to a greater or lesser degree. Such equifinality
683 has been well documented and has resulted in the development
684 of the generalized likelihood uncertainty estimation (GLUE)
685 technique, whereby many model runs are carried out, spanning
686 the likely ranges of model parameters [35]. A flood extent
687 probability map is obtained by performing a weighted average
688 of the binary-valued modeled flood extents (with the value for
689 a pixel being 1 for flooded and 0 for not flooded), with each
690 model flood extent being weighted according to its performance
691 measure relative to an observed flood extent. As previously
692 mentioned, the performance measure could be based on pat-
693 terns of height differences between observed and modeled
694 waterlines rather than on patterns of wet or dry pixels. To date,
695 the GLUE methodology has been mainly used to assess flood
696 extent uncertainty due to model parameter errors (see, e.g., [21]
697 and [36]). However, it seems a natural future step to try to
698 extend the method to cope with uncertainty in both model and
699 snake algorithm parameters [36]. Some method of limiting the
700 number of model runs that are required would probably need to
701 be employed (e.g., Gaussian emulation [37]), although some
702 reduction might result from using an improved performance
703 measure based on height differences.

VII. CONCLUSION

705   An algorithm has been developed for the automatic
706 extraction of flood extent using a snake that was generated
707 from combined SAR and lidar data, and the resulting waterline
708 compared to that generated using SAR data alone. From the re-
709 sulting snakes, sets of nodes in areas of low slope and low veg-
710 etation have been extracted, followed by further thinning. After
711 optimization of parameters, the heights of the resulting node set
712 from the snake that was conditioned on SAR and lidar matched
713 the corresponding node heights from the aerial photo waterline
714 significantly more closely than those from the snake that was
715 conditioned solely on SAR data. The conclusion is that, for
716 the variety of situations that are present in this particular

data set, the use of the lidar data has resulted in an observed waterline that varies more smoothly along the reach and is a better match to our best estimate of the true waterline heights.

REFERENCES

[1] P. D. Bates, M. S. Horritt, C. N. Smith, and D. C. Mason, "Integrating remote sensing observations of flood hydrology and hydraulic modeling," *Hydrol. Process.*, vol. 11, no. 14, pp. 1777–1795, 1997.

[2] L. C. Smith, "Satellite remote sensing of river inundation area, stage and discharge: A review," *Hydrol. Process.*, vol. 11, no. 10, pp. 1427–1439, 1997.

[3] F. T. Ulaby, R. K. Moore, and A. K. Fung, *Microwave Remote Sensing*, vol. 3. Norwood, MA: Artech House, 1986.

[4] J.-S. Lee and I. Jurkevich, "Coastline detection and tracing in SAR images," *IEEE Trans. Geosci. Remote Sens.*, vol. 28, no. 4, pp. 662–668, Jul. 1990.

[5] D. C. Mason and I. J. Davenport, "Accurate and efficient determination of the shoreline in ERS-1 SAR images," *IEEE Trans. Geosci. Remote Sens.*, vol. 34, no. 5, pp. 1243–1253, Sep. 1996.

[6] J. A. Richards, P. W. Woodgate, and A. K. Skidmore, "An explanation of enhanced radar backscattering from flooded forests," *Int. J. Remote Sens.*, vol. 8, no. 7, pp. 1093–1100, 1987.

[7] F. M. Henderson, "Environmental factors and the detection of open surface water using X-band radar imagery," *Int. J. Remote Sens.*, vol. 16, no. 13, pp. 2423–2437, 1995.

[8] S. I. Solomon, "Methodological considerations for the use of ERS-1 SAR imagery for the delineation of river networks in tropical forest areas," in *Proc. 1st ERS-1 Symp.*, Frascati, Italy, Jun. 26–27, 1995, pp. 595–600.

[9] M. S. Horritt, D. C. Mason, D. M. Cobby, I. J. Davenport, and P. D. Bates, "Waterline mapping in flooded vegetation from airborne SAR imagery," *Remote Sens. Environ.*, vol. 85, no. 3, pp. 271–281, May 2003.

[10] Y. Wang, L. L. Hess, S. Filoso, and J. M. Melack, "Understanding the radar backscattering from flooded and non-flooded Amazonian forests: Results from canopy backscatter modelling," *Remote Sens. Environ.*, vol. 54, no. 3, pp. 324–332, Dec. 1995.

[11] M. Badji and S. Dautrebande, "Characterisation of flood inundated areas and delineation of poor drainage soil using ERS-1 SAR imagery," *Hydrol. Process.*, vol. 11, no. 10, pp. 1441–1450, 1995.

[12] M. L. Imhoff, C. Vermillion, M. H. Story, A. M. Choudhury, A. Gafoor, and F. Poclyn, "Monsoon flood boundary delineation and damage assessment using space borne imaging radar and Landsat data," *Photogramm. Eng. Remote Sens.*, vol. 53, no. 4, pp. 405–413, 1987.

[13] H. Liu and K. C. Jezek, "Automated extraction of coastline from satellite imagery by integrating Canny edge detection and locally adaptive thresholding method," *Int. J. Remote Sens.*, vol. 25, no. 5, pp. 937–958, 2004.

[14] A. Niedermeier, E. Romaneessen, and S. Lehner, "Detection of coastlines in SAR images using wavelet methods," *IEEE Trans. Geosci. Remote Sens.*, vol. 38, no. 5, pp. 2270–2281, Sep. 2000.

[15] Y. Yu and S. T. Acton, "Automated delineation of coastline from polarimetric SAR imagery," *Int. J. Remote Sens.*, vol. 25, no. 17, pp. 3423–3438, Sep. 2004.

[16] P. A. Brivio, R. Colombo, M. Maggi, and R. Tomasoni, "Integration of remote sensing data and GIS for accurate mapping of flooded areas," *Int. J. Remote Sens.*, vol. 23, no. 3, pp. 429–441, Feb. 2002.

[17] G. Nico, M. Pappalepore, G. Pasquariello, A. Refice, and S. Samarelli, "Comparison of SAR amplitude vs. coherence flood detection methods—A GIS application," *Int. J. Remote Sens.*, vol. 21, no. 8, pp. 1619–1631, May 2000.

[18] M. S. Horritt, "A statistical active contour model for SAR image segmentation," *Image Vis. Comput.*, vol. 17, no. 3/4, pp. 213–224, Mar. 1999.

[19] M. S. Horritt, D. C. Mason, and A. J. Luckman, "Flood boundary delineation from synthetic aperture radar imagery using a statistical active contour model," *Int. J. Remote Sens.*, vol. 22, no. 13, pp. 2489–2507, Sep. 2001.

[20] G. Schumann, R. Hostache, C. Puech, L. Hoffmann, P. Matgen, F. Pappenberger, and L. Pfister, "High-resolution 3D flood information from radar imagery for flood hazard management," *IEEE Trans. Geosci. Remote Sens.*, vol. 45, no. 6, pp. 1715–1725, Jun. 2007.

[21] F. Pappenberger, K. Beven, M. Horritt, and S. Blazkova, "Uncertainty in the calibration of effective roughness parameters in HEC-RAS using inundation and downstream level observations," *J. Hydrol.*, vol. 302, no. 1–4, pp. 46–69, 2005.

[22] D. C. Mason, D. M. Cobby, M. S. Horritt, and P. D. Bates, "Floodplain friction parameterization in two-dimensional river flood models using vegetation heights derived from airborne scanning laser altimetry," *Hydrol. Process.*, vol. 17, no. 9, pp. 1711–1732, 2003.

[23] D. M. Cobby, D. C. Mason, M. S. Horritt, and P. D. Bates, "Two-dimensional hydraulic flood modelling using a finite element mesh decomposed according to vegetation and topographic features derived from airborne scanning laser altimetry," *Hydrol. Process.*, vol. 17, no. 10, pp. 1979–2000, 2003.

[24] G. Aronica, P. D. Bates, and M. S. Horritt, "Assessing the uncertainty in distributed model predictions using observed binary pattern information within GLUE," *Hydrol. Process.*, vol. 16, no. 10, pp. 2001–2016, 2002.

[25] D. S. Biggin and K. Blyth, "A comparison of ERS-1 satellite radar and aerial photography for river flood mapping," *J. Chart. Inst. Water Eng. Manag.*, vol. 10, pp. 1777–1795, 1996.

[26] L. M. G. Pereira and L. L. F. Janssen, "Suitability of laser data for DEM generation: A case study in the context of road planning and design," *ISPRS J. Photogramm. Remote Sens.*, vol. 54, no. 4, pp. 244–253, 1999.

[27] I. J. Davenport, N. Holden, and R. J. Gurney, "Characterizing errors in airborne laser altimetry data to extract soil roughness," *IEEE Trans. Geosci. Remote Sens.*, vol. 42, no. 10, pp. 2130–2141, Oct. 2004.

[28] D. J. Williams and M. Shah, "A fast algorithm for active contours and curvature estimation," *CVGIP, Image Underst.*, vol. 55, no. 1, pp. 14–26, Jan. 1992.

[29] J. Ivins and J. Porrill, "Statistical snakes: Active region models," in *Proc. 5th Brit. Mach. Vis. Conf.*, York, U.K., Sep. 1994, vol. 1 and 2, pp. 377–386.

[30] M. S. Horritt, "Psnake NT user manual," Univ. Bristol, Bristol, U.K., 2002. School of Geographical Sciences Report.

[31] D. C. Mason, T. R. Scott, and H.-J. Wang, "Extraction of tidal channel networks from airborne lidar data," *ISPRS J. Photogramm. Remote Sens.*, vol. 61, no. 2, pp. 67–83, 2006.

[32] C. V. Deutsch and A. Journel, *GSLIB: Geostatistical Software Library and Users's Guide*. New York: Oxford Univ. Press, 1992, p. 41.

[33] P. D. Bates, M. Wilson, M. S. Horritt, D. C. Mason, N. Holden, and A. Currie, "Reach scale floodplain inundation dynamics observed using airborne SAR imagery," *J. Hydrol.*, vol. 328, no. 1/2, pp. 306–318, 2006.

[34] S. Neelz, G. Pender, I. Villanueva, M. D. Wilson, N. G. Wright, P. D. Bates, D. C. Mason, and C. Witlow, "Using remotely sensed data to support flood modelling," *Proc. Inst. Civil Eng.*, vol. 159, no. 1, pp. 35–44, 2006.

[35] K. J. Beven and A. M. Binley, "The future of distributed models: Model calibration and predictive uncertainty," *Hydrol. Process.*, vol. 6, no. 3, pp. 279–298, 1992.

[36] M. S. Horritt, "A methodology for the validation of uncertain flood inundation models," *J. Hydrol.*, vol. 326, no. 1–4, pp. 153–165, 2006.

[37] J. E. Oakley and A. O'Hagan, "Probabilistic sensitivity analysis of complex models: A Bayesian approach," *J. R. Stat. Soc., Series B*, vol. 66, no. 3, pp. 751–769, Aug. 2004.

David C. Mason received the B.Sc. and Ph.D. degrees in physics from the University of London, London, U.K., in 1963 and 1968, respectively.

He was with the U.K. Medical Research Council and Plessey Electronic Systems Research. Since 1984, he has been with the Natural Environment Research Council Environmental Systems Science Centre, University of Reading, Reading, U.K., carrying out research on the automated extraction of information from remotely sensed data and linking these data to environmental models. His current research interests include using remotely sensed data for validation and parameterization of river flood models and assimilation into coastal morphodynamic models.

Matthew S. Horritt received the Ph.D. degree from the University of Reading, Reading, U.K., in 1998.

He was with the University of Leeds, Leeds, U.K., and the Department of Civil Engineering, University of Bristol, Bristol, U.K., as a Postdoctoral Research Fellow and a Lecturer in civil engineering, respectively. He is currently a Specialist Modeler with Halcrow Group Ltd., London, U.K. His research interests are flood inundation models, remote sensing of floods and floodplain topography, and model validation.

Tania R. Scott received the B.Sc. degree in astronomy from the University of Canterbury, Christchurch, New Zealand, in 1992 and the Ph.D. degree in astronomy from the University of Cambridge, Cambridge, U.K., in 1998.

She was with the U.K. Met Office, where she developed meteorological products for the aviation industry to address safety and environmental issues. She is currently with the Natural Environment Research Council (NERC) Environmental Systems Science Centre, University of Reading, Reading, U.K., where she is interested in using remote sensing data in aid of environmental modeling. Her current project is to apply data assimilation techniques to coastal area morphodynamic modeling, which is funded under the NERC program Flood Risk from Extreme Events.

Johanna T. Dall'Amico is currently working toward the B.Sc. degree in mathematics at the University of Reading, Reading, U.K., and a Diploma in geography and remote sensing at Ludwig-Maximilian University of Munich, Munich, Germany.

She is a Visiting Student at the Natural Environment Research Council Environmental Systems Science Centre, University of Reading, where she works on remote sensing applications for fluvial flood models.

Paul D. Bates received the Ph.D. degree from the University of Bristol, Bristol, U.K., in 1993, with support from a Natural Environmental Research Council studentship.

Subsequently, he has been with at the University of Bristol as a Postdoctoral Researcher and Lecturer, and has been a Full Professor since 2003. He is currently the Director of the Hydrology Research Group, School of Geographical Sciences, University of Bristol. He has been a Visiting Scientist at Princeton University, Laboratoire National D'Hydraulique, Paris, and the EU Joint Research Centre, Ispra, Italy. His research interests include the development and analysis of numerical models for predicting river flood flows, principally using data derived from remote sensing sources, spatial prediction, risk, and uncertainty. He is the Editor-in-Chief of the *International Journal of River Basin Management*.

Improving River Flood Extent Delineation From Synthetic Aperture Radar Using Airborne Laser Altimetry

David C. Mason, Matthew S. Horritt, Johanna T. Dall'Amico, Tania R. Scott, and Paul D. Bates

Abstract—Flood extent maps that are derived from synthetic aperture radar (SAR) images provide spatially distributed data for validating hydraulic models of river flood flow. The accuracy of such maps is reduced by a number of factors, including variation in backscatter from the different land cover types that are adjacent to the flood, changes in returns from the water surface that are caused by different meteorological conditions, and the presence of emergent vegetation. This paper describes how improved accuracy can be achieved by modifying an existing flood extent delineation algorithm to use airborne laser altimetry [light detection and ranging (lidar)] as well as SAR data. The lidar data provide an additional constraint that waterline heights should vary smoothly along the flooded reach. The method was tested on a SAR image of a flood for which contemporaneous aerial photography existed, together with lidar data of the unflooded reach. The waterline heights of the SAR flood extent that was conditioned on both SAR and lidar data matched the corresponding heights from the aerial photograph waterline significantly more closely than those from the SAR flood extent that was conditioned only on SAR data. For waterline heights in areas of low slope and vegetation, the root-mean-square error on the height differences reduced from 221.1 cm for the latter case to 55.5 cm for the former.

Index Terms—Data fusion, hydrology, lidar, snake.

I. INTRODUCTION

FLOOD extent maps that are derived from remotely sensed data are of considerable use in hydrology, providing spatially distributed data for validation of hydraulic models of river flood flow, for emergency flood relief management, and for development of spatially accurate hazard maps [1], [2]. The all-weather day–night capability of synthetic aperture radar (SAR) sensors gives these a considerable advantage for flood mapping over sensors operating at visible or infrared wavelengths, as the latter ones are unable to penetrate the cloud that often accompanies flood events. This advantage is tempered by the fact that a number of factors conspire to reduce the accuracy of flood maps that are derived from SAR imagery. These include the substantial variation in backscatter from the different land cover types that are adjacent to the flood, the changes in returns from the water surface that are caused by different meteorological conditions, the presence of emergent vegetation, and the effects of man-made structures in urban areas. This paper describes a study to reduce inaccuracies from some of these sources in an existing flood extent delineation algorithm by using an additional data source, namely, airborne laser altimetry.

The simplest model of SAR backscatter from a river flood assumes that the water surface is smoother than the surrounding land and acts as a specular reflector, reflecting radiation away from a side-looking sensor, so that the water appears dark compared to the land. Two factors complicating the simple specular reflection model in practice are the effects of wind or rain roughening of the water surface, and emergent vegetation. The relationship between SAR backscatter and surface roughness that is caused by wind blowing over the oceans is well understood [3], and the effect may raise the backscatter from the water to similar or greater levels than the adjacent land [4], [5]. Wind roughening of a river flood surface can give rise to similar effects, but these can have substantial spatial variation, depending on the local topography, which determines the fetch for a given wind direction. The presence of emergent vegetation can give rise to multiple reflections between the water and the vegetation, leading to a substantial enhancement of backscatter, the magnitude of which is a function of radar wavelength, look angle, and polarization. The effect has been observed in a number of studies of flooded forest and marshland (e.g., [6]–[9]), and the increase in backscatter has been modeled mathematically in [10]. Enhanced backscatter from the water surface that is caused by wind roughening or emergent vegetation will also result in an increased level of noise due to the multiplicative nature of noise in SAR images.

A number of methods for the automated delineation of flood extent in SAR imagery of both fluvial and tidal environments have been developed [4], [5], [9], [11]–[21]. Several of these studies have illustrated the great potential of SAR sensors for synoptic observation of large flooding events. An automatic technique for delineating a fluvial flood using a statistical active contour model (or snake) that is applied to a SAR image to identify areas of homogeneous speckle statistics is described in [18] and [19]. This assumes that single-frequency single-polarization SAR intensities are available and was aimed at producing an observed flood extent against which to validate

a modeled flood extent. Due to the difficulties of imaging urban areas using SAR, its use is limited to large-area mapping of floods in rural areas. The SAR segmentation uses both local tone and texture measures, and is capable of accurate feature boundary representation. The method was applied to a flood that was imaged using the ERS-1 satellite SAR sensor and proven to be capable of identifying 75% of the flooded area correctly, with 70% of the waterline coinciding with ground data within 20 m. The main error in waterline position was found to be due to unflooded short vegetation that was adjacent to the flood giving similar radar returns to open water, causing an overestimation of flood extent. The loss of flood extent due to emergent vegetation was found to be a secondary source of error.

Further work on this topic [22], [23] found that, as a result of these error sources and the relatively large size of the European Remote Sensing Satellite (ERS) SAR pixel, the heights of the SAR waterline along a flooded reach could sometimes be in error by several meters (although, generally, it was much less) and could exhibit significant noise. One reason for this was that there was no constraint that the waterline heights should vary smoothly along the reach, whereas, in reality, the longitudinal slope of typical flood flows is low $(\sim 0.001-0.0001 \ \mathrm{m} \cdot \mathrm{m}^{-1})$, and changes in slope are very gradual. With this level of differences, the SAR image becomes much less useful for model flood extent validation than it could otherwise be.

Horritt *et al.* [19] point out that their flood extent mapping procedure identifying the flood as a region of relatively homogeneous speckle statistics may be improved by the adoption of a model-based approach. In this vein, this paper describes the use of light detection and ranging (lidar) data to modify the SAR waterline, so that it becomes more useful for validation. The snake algorithm [18], [19] is modified to look not only at SAR image space but also at lidar digital terrain model (DTM) and vegetation height maps, so that the snake can be conditioned to be smoothly varying in ground height as well as in SAR intensities and textures. This should reduce errors that are caused by unflooded vegetation that is adjacent to the flood giving similar returns to open water and also errors due to the SAR pixel size. It could also help somewhat in reducing errors due to emergent vegetation. An additional benefit of producing a more smoothly varying waterline is that it may allow the development of improved performance measures for flood extent validation based on patterns of height differences rather than on patterns of wet or dry pixels, as currently done [24]. The algorithm specifically sets out to improve the vertical accuracy of the SAR waterline, although any improvement should also lead to improvement in the horizontal waterline accuracy due to their correlations that are contained within the DTM.

Used in this way, the lidar data may actually play a dual role in the modeling process, as lidar is often used to parameterize the hydraulic model being validated, with the lidar DTM providing the model bathymetry and possibly the vegetation heights being used to estimate bottom friction [22]. However, the use of lidar data in SAR waterline extraction as well as model parameterization does not under-
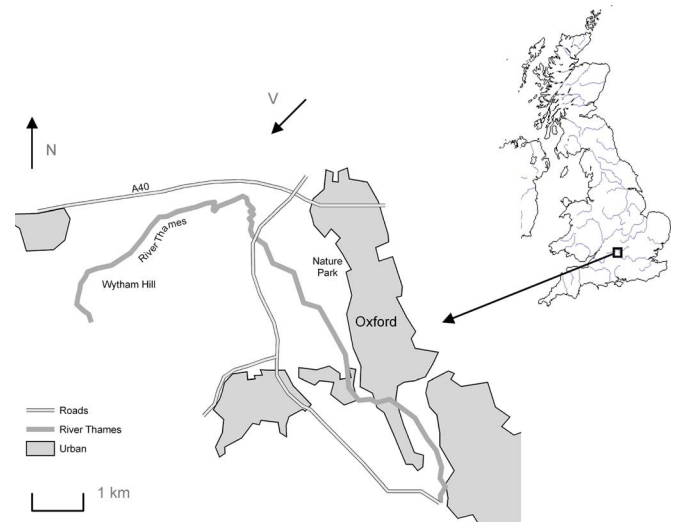

Fig. 1. Location of the test area.

mine the independence of the SAR waterline in the validation process.

II. TEST DATA SET

An ideal data set on which to validate the method would be from a flood for which both satellite SAR data and simultaneous aerial photography were available, so that the SAR snake waterlines that are conditioned without and with the lidar data could be compared with the waterline from the aerial photographs. In addition, lidar data of the unflooded area should be available.

Biggin and Blyth [25] acquired oblique aerial photos of a flood on the Thames west of Oxford, U.K., on December 4, 1992, at the same time (to within 2 h) as an ERS-1 SAR overpass of the area. The Thames is a low-relief slow-response catchment, and at this point along its course, the river discharge during a flood changes only very gradually, so that such timing differences are unimportant. The peak discharge for this event was measured at 76 $\mathrm{m}^3 \cdot \mathrm{s}^{-1}$, which represents a $\sim$1-in-5-year-recurrence interval flow. The ERS-1 SAR image was acquired approximately 36 h after the flood peak when the discharge had dropped to 73 $\mathrm{m}^3 \cdot \mathrm{s}^{-1}$, indicating the very slow response of the catchment. At the time of overpass, there was no wind or rain in the area. The location of the test area is shown in Fig. 1, and an example of the aerial photography is shown in Fig. 2. The floodplain over this reach is semirural, with the majority of fields being used at the time for pasture or having been ploughed. There are also several urban areas, and the region is crossed by a number of major roads and railways. The flood waterline was delineated by eye from the aerial photos and vectorized [19]. The waterline vectors were then georeferenced using an orthographic transform that is parameterized by a least squares method using 15–20 control points for each photograph. The error in the waterline position was assessed from waterline segments where the waterline was observed to lie alongside a hedgerow or field boundary that could be located on a 1 : 25 000 scale map and was found to be less than 20 m.

Fig. 2. Example of the aerial photography in the upper section of the reach, looking southwest from the north of the region (the view direction is V in Fig. 1).

180 Lidar data at 1-m resolution were acquired for a section
181 of this reach west of Oxford and approximately 12 km long
182 by the Environment Agency of England and Wales (EA). The
183 lidar was an Optech ALTM 2033 that was flown on a Cessna
184 aircraft at 120 kn at a flying height of 900 m, with a laser
185 firing rate of 33 kHz, a scanning frequency of 30 Hz, and a
186 scanner half angle of 18°. The lidar heights were validated by
187 the EA by comparing them with a set of global positioning
188 system (GPS) heights of several flat unvegetated surfaces in
189 the area. Based on a sample of 299 GPS readings, the lidar
190 heights were found to have an rms error of 10.6 cm, which
191 comprised a random error of 10.2 cm and a systematic error
192 of 2.6 cm. Lidar height accuracy reduces on steeper slopes
193 and in vegetated regions [26]. Lidar positional accuracy was
194 about 0.4 m [27]. The postprocessed lidar DTM and vege-
195 tation height mask were obtained from the EA. These were
196 degraded to 2-m pixel size to avoid too large a mismatch
197 with the SAR pixel size of 12.5 m. Fig. 3 shows the lidar
198 DTM with the high land of Wytham Hill in the west and the
199 raised Oxford Nature Park in the east (see Fig. 1), both of
200 which are relevant to this study. Fig. 3 also shows the aerial
201 photo waterline overlain on the lidar DTM, with the waterline
202 color representing its difference in height from the local mean
203 waterline height (within 0.5-km distance). The presence of
204 large sections of waterline having small differences (blue color)
205 from the local mean height indicates that the aerial waterline
206 height varies smoothly along the reach. The waterline includes
207 instances of islands of higher ground that are surrounded by
208 water. It is assumed here that all areas of water have been
209 accurately mapped, so that the validation data are essentially
210 error free.

III. Flood Extent Extraction From SAR Data 211

A. Algorithm Description 212

A detailed description of the algorithm to delineate a flood 213
using an active contour model is given in [18], and only an 214
overview is presented here. Active contour models or snakes 215
are useful for converting incomplete or noisy edge maps into 216
smooth continuous vector boundaries [5], [28]. The edge image 217
space is searched using a dynamic curvilinear contour that is 218
driven to be attracted to edge pixels using an energy minimiza- 219
tion function, so that the contour can link together unconnected 220
edge segments. The contour (snake) is represented in a piece- 221
wise linear fashion as a set of nodes (i.e., the coordinates of the 222
snake points) that are linked by straight-line segments. Ivins 223
and Porrill [29] developed a statistical snake that operates on 224
the image itself rather than an edge image, dispensing with the 225
need for a prior edge detection stage. Their technique involves 226
estimating the local image mean intensity (tone) at a node using 227
the pixels between this node and its adjacent nodes. This gives 228
the advantage that noise due to SAR speckle is reduced by 229
averaging pixel intensities along an edge while, at the same 230
time, maintaining resolution that is perpendicular to the edge, 231
giving accurate edge positioning. The local intensity variance 232
(texture) is also calculated from these pixels, as this has proven 233
to be a useful discriminator between different natural land- 234
cover types having similar mean intensities in SAR imagery. 235

The statistical snake is formulated as an energy minimization 236
problem with the total snake energy $E(\boldsymbol{u}(s))$ given by 237

$$E\left(\boldsymbol{u}(s)\right) = E_{\text{tension}} + E_{\text{curvature}} - \iint G\left(I(x,y)\right) dx\, dy \quad (1)$$
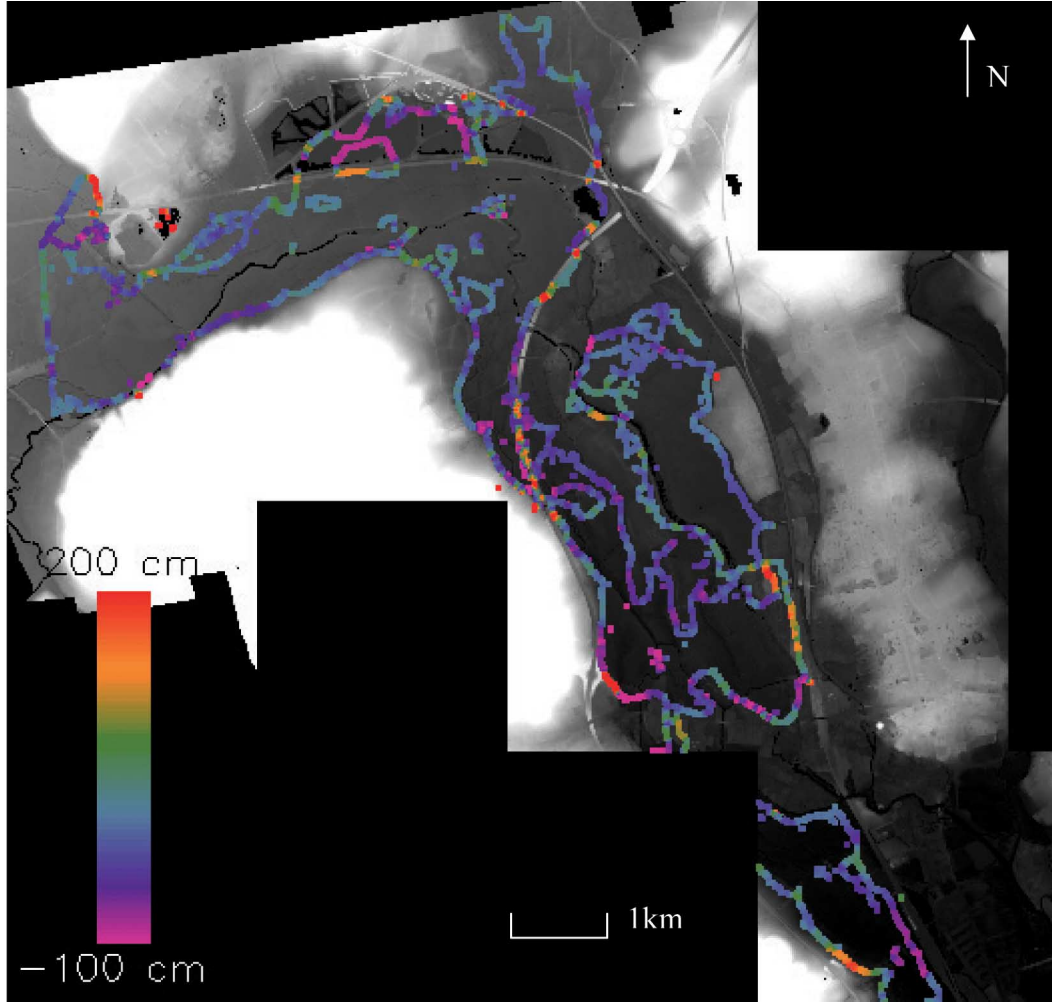
4/C   Fig. 3.   Aerial photo waterline overlain on the lidar DTM. The colors represent the difference in height of the waterline from the local mean waterline height.

where $\boldsymbol{u}(s) = (x(s), y(s))$ describes the contour position (x, y) in the 2-D image space as a vector function of arc length parameter s. E_{tension} and $E_{\text{curvature}}$ are energies that are generated by the model's internal tension and stiffness constraints, which favor a smooth uncrenellated contour that is made up of evenly spaced nodes (see the following). G is a goodness function that assesses how well a set of image pixels $I(x, y)$ meets certain criteria. The total energy is minimized if the contour encloses a region of pixels that is homogeneous in tone and texture.

If the mean and variance of the intensities of the set of pixels that are immediately at either side of a particular snake node are measured, the knowledge of how these variables are distributed can be used to estimate the probability that these pixels match those that are already within the region that is enclosed by the contour. Horritt [18] relates G to the log of this probability, with the dependence on the measured sample mean μ', for example, having the form

$$G(\mu') = 1 - n(\mu' - \mu)^2 / v k^2 \qquad (2)$$

where μ and v are the mean and variance of the seed population that is already enclosed within the contour, respectively; n is

the sample size; and k is a parameter that can be adjusted to tune algorithm performance. G is then equal to 1 for a set of pixels with the expected mean but falls to zero if the mean differs by $k\sqrt{(v/n)}$ (i.e., k standard deviations) from the expected value. The parameter k is usually set at about 2 or 3 but may be increased further to allow for a level of statistical inhomogeneity in the region being segmented. The overall goodness function (with components that are based on both the measured mean and variance) is limited to a minimum value of -1.

The roles of the tension and curvature constraints are to produce a contour of appropriate smoothness with evenly spaced nodes, by a consideration of the balance between image and curvature forces. Consider the situation that is shown in Fig. 4 for snake nodes at $\boldsymbol{u}_{i-1}$, $\boldsymbol{u}_i$, and $\boldsymbol{u}_{i+1}$ that are linked by unit vectors $\boldsymbol{v}_i$ and $\boldsymbol{v}_{i+1}$. The local curvature is $\Delta\theta/\Delta s$, where $\Delta\theta$ is the change of angle along arc length Δs. Horritt [18] gives the contribution to the total curvature energy as

$$\Delta E_{\text{curvature}} = \gamma (\Delta\theta/\Delta s)^2 / \Delta s = \gamma |\boldsymbol{v}_{i+1} - \boldsymbol{v}_i|^2 / a_i \qquad (3)$$

where a_i is the distance between the midpoints of $\boldsymbol{v}_i$ and $\boldsymbol{v}_{i+1}$, and γ is a curvature energy weighting parameter. Equation (3)
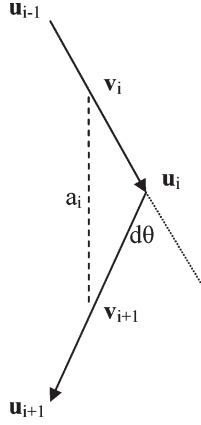
Fig. 4.   Vectors for describing curvature and tension energies (after [18]).

278 is valid for small values of $\Delta\theta$. Similarly, the contribution to
279 the tension energy is given by

$$\Delta E_{\text{tension}} = \lambda \left(|\boldsymbol{u}_{i+1} - \boldsymbol{u}_i|^2 + |\boldsymbol{u}_i - \boldsymbol{u}_{i-1}|^2 \right) \qquad (4)$$

280 where λ is the tension energy weighting parameter. The mag-
281 nitudes of these energies can be adjusted using the weighting
282 parameters. Too large a value for the curvature parameter
283 will make the curvature term dominate the model energy and
284 produce an unrealistically smooth contour. Too large a value of
285 the tension parameter will favor a short contour and stifle the
286 growth of the snake.
287   The scheme that was used to minimize the energy is the
288 algorithm of Williams and Shah [28]. For each node at each
289 iteration, the change in energy dE is computed for moves to all
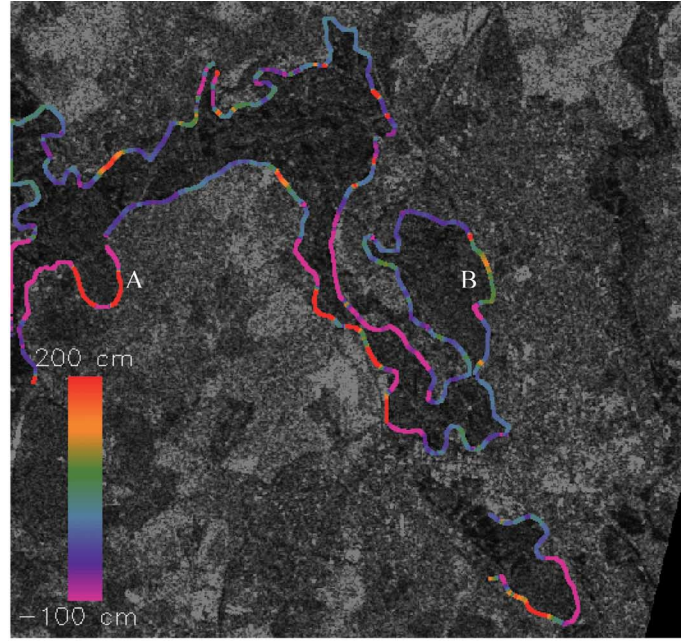290 eight neighbors of the node

$$dE = -GdA + dE_{\text{tension}} + dE_{\text{curvature}}. \qquad (5)$$

291   The lowest (most negative) dE is chosen. Obviously, dE is
292 equal to zero for no node movement. G is calculated along the
293 line segments linking the node with its two neighbors, and dA is
294 the local change in area. If G is positive, the snake is in a region
295 of homogeneous pixels, a positive dA is favored, and the snake
296 expands. If G is negative, the snake is in an inhomogeneous re-
297 gion, a negative dA is favored, and the snake retreats. The mean
298 and standard deviation of the seed population are calculated
299 from all pixels lying inside the contour every ten iterations.
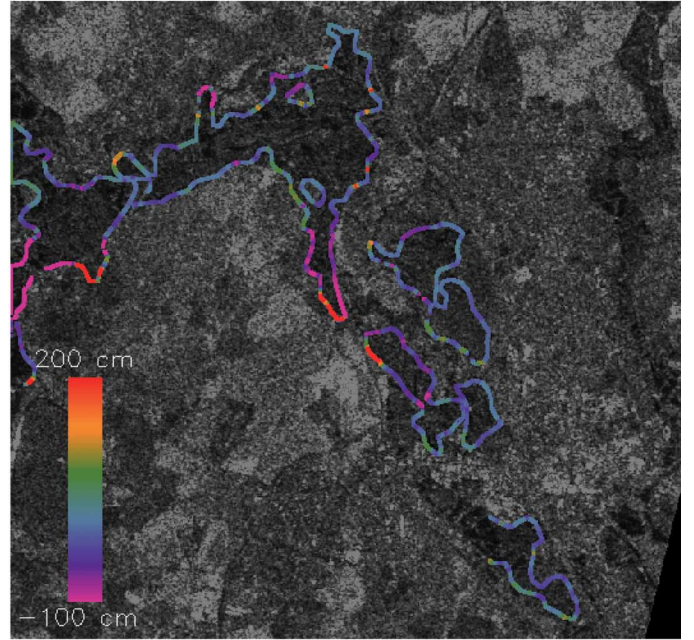300   The flooded region may not be simply connected, as islands
301 and isolated water bodies may form holes and outliers. To cope
302 with this, the algorithm incorporates a method for dealing with
303 complex topology and snake self-intersection. As an example,
304 a snake may spawn a smaller subsnake within itself to represent
305 an island.

B. Implementation and Qualitative Assessment of Results

307   A personal computer (PC)-based implementation of the al-
308 gorithm (Psnake NT) was used in this paper [30]. Psnake NT
309 is a software package that is available to the hydrological
310 modeling community for the semiautomatic extraction of flood

(a)

(b)

Fig. 5.   Waterline conditioned only on SAR data overlain on SAR data (a) for 4/C
parameter $k = 3$ and (b) $k = 2$. The colors represent the difference in height
of the waterline from the local mean waterline height.

extents from SAR data. Fig. 5 shows snake waterlines that are 311
generated using SAR data only, for the number of standard 312
deviations k of 3 and 2, overlain on SAR data. It has been found 313
by experiment that k is probably the most important parameter 314
controlling the snake [19]. Other parameter settings were a 315
minimum node spacing of 6 pixels, a maximum node spacing 316
of 12 pixels, curvature parameter γ of 68.3, tension parameter λ 317
of 0.1, a texture weight of 0.2, and iterations of 200. The snake 318
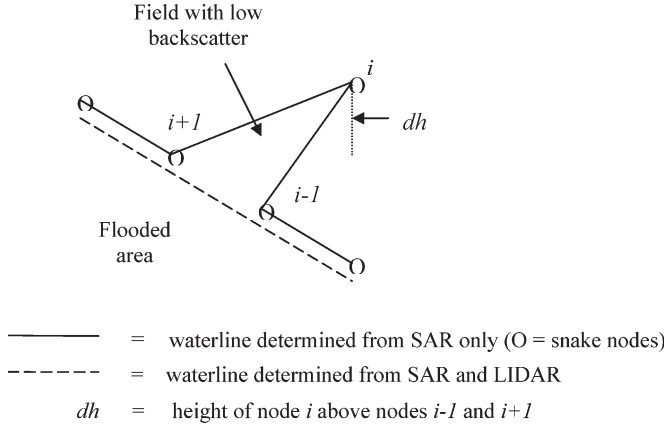was seeded (i.e., initialized) manually as a narrow strip lying 319

Fig. 6.   Example error that might be corrected using lidar.

along the course of the unflooded river channel, ensuring that it contained only flooded pixels.

In Fig. 5, the snake shows a tendency to leak onto higher ground on Wytham Hill [point A in Fig. 5(a), see also Fig. 3]. This is likely to be due to the presence of vegetated fields, which correspond to areas of low SAR backscatter and are likely to be misclassified as flooded. While no ground reference data were acquired at the time of the flood, evidence for this comes from a recent aerial photograph that was obtained later than the SAR image. A further example of leakage of the snake onto higher ground is visible at point B in Fig. 5(a), where the snake has leaked onto the Oxford Nature Park, which is higher than the land toward the Thames yet again exhibits low SAR backscatter.

IV. FLOOD EXTENT EXTRACTION FROM SAR AND LIDAR DATA

A. Algorithm Modification

The snake algorithm was modified so that the snake was conditioned not only on the SAR image but also on the lidar DTM, so that it becomes smoothly varying in ground height as well as in SAR intensities and textures. The principle that was adopted was that the SAR image should still be the primary determinant of the flood extent. In most areas, the flood extent that was determined by the SAR will be correct within the SAR resolution, but where errors creep in the lidar can help to correct these.

The lidar DTM is able to provide a ground height at each pixel, so that each position $u(x, y)$ becomes $u(x, y, z)$. The modification involves using the lidar heights to measure curvatures and tensions at snake nodes in 3-D rather than 2-D space. Consider an instance where an unflooded field with low SAR backscatter is adjacent to a flood edge, such that the field is included in the SAR waterline determined by the snake (Fig. 6). As there will likely be a rise in height (dh) across the field that is perpendicular to the true flood edge, the error in the waterline will give rise to a significant component of curvature in the vertical plane, which will not be present in the waterline segments that are adjacent to the field. To be specific, in Psnake

NT, the contribution to the 3-D curvature energy at the snake node at $u(x_i, y_i, z_i)$ from its two adjacent nodes is

$$\Delta E_{\text{curvature}} = \gamma |v_{i+1} - v_i|^2 / a_i = \left(c_{ix}^2 + c_{iy}^2 + c_{iz}^2 \right) / a_i \quad (6)$$

where

$$c_{ix} = (x_{i+1} - x_i)/d_{i+1} - (x_i - x_{i-1})/d_i$$
$$c_{iy} = (y_{i+1} - y_i)/d_{i+1} - (y_i - y_{i-1})/d_i$$
$$c_{iz} = (z_{i+1} - z_i)/d_{i+1} - (z_i - z_{i-1})/d_i$$
$$d_i = \left((x_i - x_{i-1})^2 + (y_i - y_{i-1})^2 + (z_i - z_{i-1})^2 \right)^{0.5}$$
$$d_{i+1} = \left((x_{i+1} - x_i)^2 + (y_{i+1} - y_i)^2 + (z_{i+1} - z_i)^2 \right)^{0.5}$$
$$a_i = \Big(((x_{i+1} + x_i)/2 - (x_i + x_{i-1})/2)^2$$
$$+ ((y_{i+1} + y_i)/2 - (y_i + y_{i-1})/2)^2$$
$$+ ((z_{i+1} + z_i)/2 - (z_i + z_{i-1})/2)^2 \Big)^{0.5}$$

and the suffixes refer to the node numbers in Fig. 6. To reduce the vertical curvature component c_{iz}^2 at node i in Fig. 6, the snake will try to contract to drag node i back to be collinear with nodes $i - 1$ and $i + 1$, which will also reduce c_{ix}^2 and c_{iy}^2. The 3-D tension energy, which is proportional to $(d_{i+1}^2 + d_i^2)$, will also be reduced by this move.

A waterline error due to the presence of emergent vegetation at the edge of the flood might also have significant components of vertical curvature and tension that could be reduced by correcting the error. A complicating factor in this case is that the SAR and lidar forces might be acting against each other. In order to reduce the vertical curvature and tension by incorporating the area of enhanced backscatter into the flooded area, the inhomogeneity of the SAR returns in the flooded area would generally have to increase. Which force won out in a particular case would depend on their relative strengths. However, this effect is not the dominant source of error [19].

In order to take account of the fact that a change in height at a node should, in general, cause different changes in curvature and tension compared to the same magnitude change of node position in the xy plane, the lidar heights were scaled by weighting factor w_l with respect to the (x, y) coordinates.

The straightforward approach to combining the SAR and lidar data would be to use the existing algorithm with both data sets and simply calculate 3-D rather than 2-D curvature and tension energies. A possible objection to this might be that, if there were flooded mounds in the floodplain that are not visible to the SAR but visible to the lidar, these might retard the expansion of the snake and distort the eventual waterline. An alternative approach could be to use the algorithm with SAR data and 2-D curvatures and tensions only initially. Then, the snake iterations could continue using SAR and lidar data, and 3-D curvatures and tensions, causing the snake to adjust itself to correct errors where necessary. However, in cases where the waterline was significantly in error, it might be difficult to recover from these errors. For example, if the snake leaked onto higher ground, it might be impeded from returning to the true waterline position by a hollow in the higher ground. In practice, it turns out that the straightforward approach using

400 the existing algorithm and calculating 3-D curvatures and ten-
401 sions works well enough.
402 The SAR data may have significantly lower resolution than
403 the airborne lidar data, as in the present test data set comprising
404 ERS satellite SAR data. In this case, it may be possible to
405 correct the waterline position to sub-SAR pixel accuracy in a
406 second pass of the algorithm. The idea would be to rescale the
407 SAR image and the snake waterline from the first pass to the
408 higher resolution of the lidar, and to continue iterating to try to
409 move the snake nodes away from the centers of the enlarged
410 SAR pixels to create a waterline varying more smoothly in
411 height along its length. A constraint would be that a node should
412 not be allowed to move outside its enlarged SAR pixel, as no
413 further information could be extracted from the SAR image at
414 this stage.

415 *B. Implementation and Qualitative Assessment of Results*

416 For the first pass of the modified algorithm, the lidar image
417 was degraded to the same pixel size as the SAR image (12.5 m)
418 by averaging the lidar heights within each SAR pixel. The
419 parameter settings for this pass were the same as those for the
420 snake that was conditioned on only the SAR data (other than for
421 k and w_l). The initial value of lidar weight factor w_l was chosen
422 by experiment to be 0.15. This took into account the fact that
423 the leakage at Wytham Hill [at point A in Fig. 5(a)] occurs over
424 a distance of about 0.5 km. Curvature at a node is calculated
425 using the two adjacent nodes on either side of the central node,
426 spanning four internode spacings. For an internode spacing of
427 eight pixels, this corresponds to a distance of about 400 m,
428 roughly matching that required. The w_l setting also reflected
429 the facts that the lidar heights were expressed in millimeters
430 and that a, for example, 1000-mm rise in the lidar height of the
431 central node should give rise to a significant increase in 3-D
432 curvature. Even though a node can only be moved horizontally
433 by one SAR pixel at each iteration, this still amounts to a
434 horizontal shift of 12.5 m, which is large compared to a 1-m
435 vertical rise.
436 The original snake seed that was used contained only pixels
437 south of the A40 road west of Oxford (Fig. 1), and it was
438 found on the first pass that, with the 3-D curvature constraint,
439 the snake would not expand into the flooded areas north of the
440 embanked road, even though this was, on average, only 1.5 m
441 higher than the fields surrounding it. In practice, floodwater
442 from the Thames flows under the A40 onto the lower land
443 to the north through culverts that are spaced at about 250-m
444 intervals. To overcome this difficulty, additional snake seed
445 pixels were inserted to the north of the A40, which were
446 then able to expand into the northernmost part of the flooded
447 region. The same snake seed was used for all snakes that
448 were generated, whether they were conditioned using the lidar
449 data or not.
450 The second pass took place at higher resolution, i.e., at the
451 2-m pixel spacing of the lidar data. The input to this pass was
452 the snake output from the first pass, with the node coordinates
453 scaled up by 6.25 to match the change in resolution. The
454 SAR image was interpolated from 12.5 to 2 m using nearest
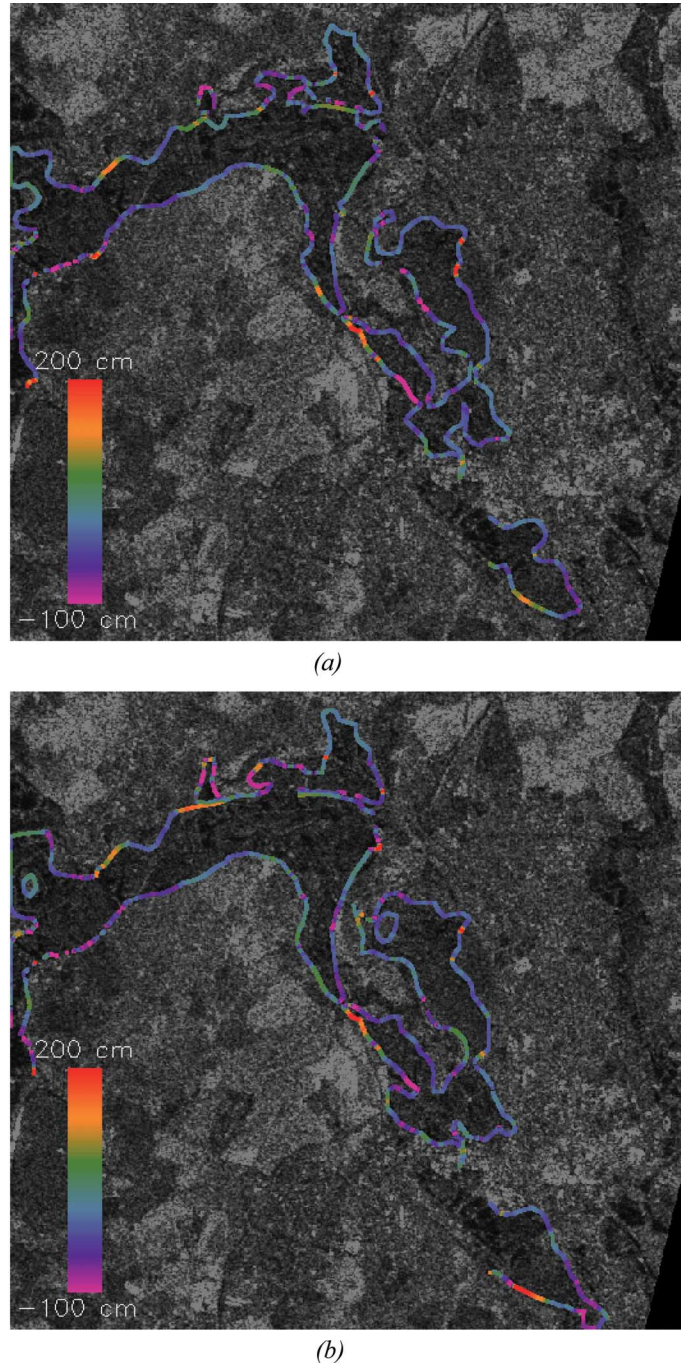455 neighbor interpolation. The number of iterations was set to 3,

(a)

(b)

Fig. 7. Waterline conditioned on SAR and lidar data overlain on SAR data **4/C**
(a) for parameter $k = 3$ and $w_l = 0.15$, and (b) for $k = 4$ and $w_l = 0.15$.
The colors represent the difference in height of the waterline from the local
mean waterline height.

to ensure that the snake nodes would not move outside the SAR 456
pixels within which they had stabilized after the first pass. The 457
minimum and maximum node spacings were also upscaled to 458
37 and 74 pixels, respectively, ensuring similar 3-D curvatures 459
to those on the first pass. 460
Fig. 7 shows snake waterlines that were conditioned on both 461
SAR and lidar data, for k values of 3 and 4 and lidar weight 462
$w_l = 0.15$, overlain on 12.5-m SAR data. It is clear that the 463
tendency for the snake to leak to higher ground at Wytham Hill 464
and at the Oxford Nature Park has been much reduced (see 465

also Fig. 3). A further benefit is that the snake appears to be more stable to parameter changes. For example, in Fig. 5, the snake that was conditioned only on SAR data shows substantial change when k is raised from 2 to 3, whereas in Fig. 7, the snake that was conditioned on SAR and lidar shows less change when k is raised from 3 to 4. This finding is born out more rigorously in the quantitative analysis described in the next section.

The main errors in waterline position that were corrected using the lidar data are due to the unflooded short vegetation that is adjacent to the flood giving similar returns to open water. The ability of the algorithm to correct loss of flood extent due to emergent vegetation is hardly tested using this data set, as this has few significant examples. The most obvious instances are emergent hedges between adjacent flooded fields, but these are generally of insufficient area to stop the snake subsuming them into its interior, even if conditioned only on SAR data.

V. PARAMETER OPTIMIZATION AND QUANTITATIVE COMPARISON OF METHODS

The snake parameters were optimized using a quantitative measurement of algorithm performance. The snake and aerial photo waterlines were first heighted by superimposing them on the lidar DTM. The snake waterline is defined only at the snake nodes. Only nodes on low slopes and in areas of short vegetation in the lidar vegetation height map were selected for heighting, as these are the ones that are likely to be heighted most accurately. The lower the slope, the smaller the node height error for a given error in its position. No requirements were made that selected nodes should have a strong SAR edge [indicated by a low G value (2)] associated with them, as this would reject nodes at the boundaries between the flood and an unflooded field giving low SAR backscatter, or between a region of emergent vegetation at the flood edge and an adjacent unflooded land (both giving high SAR backscatter).

For each snake node that was selected, the aerial photo height to associate with the snake height was found by finding the height of the closest aerial photograph waterline point. This was found by applying a distance-with-destination transform to the aerial photo waterline image. The distance-with-destination transform is a form of distance transform that stores, for each pixel in the transform image, its distance to the nearest waterline point and also the direction from which the minimum distance was propagated. This allows backtracking from a pixel to find its nearest waterline point [31]. Corroborating the finding of [19], the average separation distance was about 50 m, although this value was strongly influenced by a small number of pairs having large separations, and the average separation of 70% of the pairs having separations of less than 50 m was only 20 m. However, the pairs with large separation were not rejected, as they included examples where, e.g., the SAR waterline was displaced from the aerial photo waterline by a complete field width due to misclassification of the field as flooded. The anticipation was that these events would be less common when the snake was conditioned on the SAR and lidar data than on the SAR data alone.

Parameters were optimized by minimizing the sum of the squared height differences between the snake nodes and their corresponding aerial photo waterline points. To ensure that adjacent pairs of heights were largely uncorrelated, the pairs that were selected so far were thinned further, so that no pair was closer than 200 m to another. This distance was estimated by constructing a correlogram from the set of pairs [32] and was the distance at which the average correlation between adjacent pairs became less than 0.2. From the remaining pairs, the mean and standard deviations of the snake and aerial photograph waterline heights were calculated, as was the rms error of the height differences, with this being the variable to minimize in the parameter optimization. The mean height difference and the standard deviation of the differences were also calculated, and this allowed a paired t-test to be performed to test whether the differences were significantly nonzero. The paired t-test is used to exploit the fact that, while corresponding SAR and aerial photograph waterline heights will be correlated due to the gradual drop in height along the reach, the height differences at corresponding nodes will be uncorrelated due to the thinning process, as required by the paired test.

Only the most important parameters were investigated in the optimization procedure. For the snake that was conditioned on only SAR data, the parameter that was optimized was k. For the snake that was conditioned on SAR and lidar data, k and w_l were optimized.

Table I(a) shows the results of varying k for the snake that was conditioned on only the SAR data. The minimum rms error is 221.1 cm, which was obtained for $k = 2.0$. The associated high t value implies that there is a significant height difference at the 5% level between the snake and aerial photo waterlines. The corresponding snake is shown in Fig. 5(b). Higher values of k give significantly larger rms errors, and the high t values that were coupled with positive mean height differences imply that, for all these k values, the snake waterline heights are significantly higher than those of the aerial photograph.

Table I(b) shows the results of varying k for the snake that was conditioned on SAR and lidar data, with w_l held constant at 0.15. The minimum rms error is 55.5 cm, which was obtained for $k = 3.0$. The associated t value is not significantly nonzero, so that there is no significant difference between the snake and aerial photo waterline heights. The corresponding snake is shown in Fig. 7(a).

Table I(c) shows the results of varying w_l for the snake that was conditioned on SAR and lidar data, with k held constant at 3.0. The minimum rms error is obtained at $w_l = 0.15$. Over the ranges of k and w_l that were investigated, none of the t values are significantly nonzero, implying greater robustness to parameter changes than the case for the snake that was conditioned on only SAR data.

Table II gives the frequency tables of the absolute differences of the paired heights for the parameter sets giving the minimum rms errors for the snake that was conditioned on only the SAR data and the snake that was conditioned on SAR and lidar data. It can be seen that the increase in the rms error in the case of the snake that was conditioned only on SAR data is due almost entirely to the large number of pairs having height differences of greater than 300 cm. This is also apparent in Fig. 8, where the paired height differences for the two cases are plotted as a

TABLE I

RESULTS OF (a) VARYING k FOR THE SNAKE CONDITIONED ON ONLY THE SAR DATA, (b) VARYING k FOR THE SNAKE CONDITIONED ON SAR AND LIDAR DATA, WITH w_l HELD CONSTANT AT 0.15, AND (c) VARYING w_l FOR THE SNAKE CONDITIONED ON SAR AND LIDAR DATA, WITH k HELD CONSTANT AT 3.0

k	Number of height pairs	R.m.s. error in height (cm)	Mean height difference (cm)	t_0	Probability $t > |t_0|$ (one-sided test)	Relative height standard deviation (cm)
1.5	165	238.8	31.6	1.7	0.04	105.3
2.0	200	221.1	33.7	2.2	0.02	136.2
2.5	197	381.3	65.4	2.4	0.01	263.1
3.0	195	331.4	64.5	2.8	0.004	314.4
4.0	206	317.5	70.7	3.3	0.0005	379.1

(a)

k	Number of height pairs	R.m.s. error in height (cm)	Mean height difference (cm)	t_0	Probability $t > |t_0|$	Relative height standard deviation (cm)
2.8	195	57.8	-1.5	-0.4	0.35	43.5
3.0	191	55.5	-4.3	-1.0	0.15	42.6
3.2	190	86.6	-3.1	-0.5	0.30	52.6
3.5	195	120.8	5.2	0.6	0.28	65.4
4.0	195	63.7	4.5	1.0	0.15	48.9

(b)

w_l	Number of height pairs	R.m.s. error in height (cm)	Mean height difference (cm)	t_0	Probability $t > |t_0|$	Relative height standard deviation (cm)
0.10	187	90.2	-0.1	-0.1	0.46	47.4
0.14	196	61.0	5.4	1.2	0.10	43.0
0.15	191	55.5	-4.3	-1.0	0.15	42.6
0.16	191	55.8	0.7	0.2	0.42	43.5
0.20	195	81.5	-9.0	-1.5	0.07	54.7

(c)

TABLE II

FREQUENCY TABLES OF THE ABSOLUTE DIFFERENCES OF PAIRED HEIGHTS FOR THE PARAMETER SETS GIVING THE MINIMUM RMS ERRORS FOR THE SNAKE CONDITIONED ON ONLY THE SAR DATA AND THE SNAKE CONDITIONED ON SAR AND LIDAR DATA

	0-49cm	50-99cm	100-149cm	150-199cm	200-249cm	250-299cm	300-499cm	>=500cm
Snake conditioned on SAR data ($k = 2.0$)	155	20	9	3	3	1	3	6
Snake conditioned on SAR and LiDAR data ($k = 3.0$, $w_l = 0.15$)	154	20	9	5	2	1	0	0

VI. DISCUSSION

The method may be applied to the validation of the flood models of other river reaches, with the only prerequisites additional to the usual data required to set up a hydraulic model (e.g., an inflow hydrograph and river channel cross-sectional data) being the availability of SAR imagery of the river in flood and reasonably contemporaneous lidar data of the unflooded reach. It would be relatively straightforward to make the procedure operational. Lidar data are now often used to parameterize the hydraulic model, making it more likely that they would also be available to improve the SAR waterline. It would be straightforward to implement the modified algorithm within the Psnake NT software package. For this catchment, the algorithm processing time was less than 1 min on a Pentium IV personal computer.

The emphasis in the foregoing has been on ERS satellite SAR data because of the availability of simultaneous ERS SAR and aerial photography of the 1992 Oxford flood. While ERS SAR data have poorer resolution than airborne lidar data, the technique should also be applicable in cases where the SAR resolution is similar to that of the lidar (e.g., airborne SAR), in which case a second pass of the algorithm would certainly be unnecessary. The algorithm of [18] and [19] has been used to delineate flood extents in airborne SAR imagery [33], [34]. However, given the increasing number of satellite SAR sensors flying or planned and the difficulty of flying aircraft in poor weather often accompanying floods, satellite SARs are likely to remain to be a major source of SAR data for flood mapping in the future. While the ERS SAR sensor has single VV polarization and a fixed $23°$ viewing angle, the advent of later sensors with higher resolutions, multiple polarizations, and variable viewing angles (e.g., RADARSAT and Envisat Advanced SAR) has allowed improved flood delineation (e.g., [15]). The high-resolution satellite SAR sensors due for launch shortly (e.g., RADARSAT-2, TerraSAR, and the Cosmo-Skymed constellation) will have resolutions that match or almost match that of airborne lidar.

Production of a more smoothly varying waterline may allow the development of improved performance measures for flood extent validation based on patterns of height differences between observed and modeled waterlines rather than on patterns of wet or dry pixels, as currently done. Aronica *et al.* [24]

function of distance downstream. The main effect of the lidar data is to correct errors in the sections of waterline containing these outliers, when the snake is conditioned on both SAR and lidar.

The effect of the second pass of the algorithm in correcting the waterline position to sub-SAR pixel accuracy was also assessed. For the parameter set giving the minimum rms error for the snake that was conditioned on SAR and lidar data ($k = 3.0$ and $w_l = 0.15$), the algorithm was run for only the first pass. The minimum rms error was 58.1 cm, which is only slightly higher than the 55.5 cm that was achieved when both passes were employed. There was slightly more difference when k was raised to 4.0 and when the rms error increased to 70.8 from 63.7. This indicates that the main reduction in error is being generated in the first pass and that the second gives only a second-order improvement. This may be partly because only snake nodes on low slopes have been selected, and thus, height differences across the SAR pixel, due to its size, will be small.
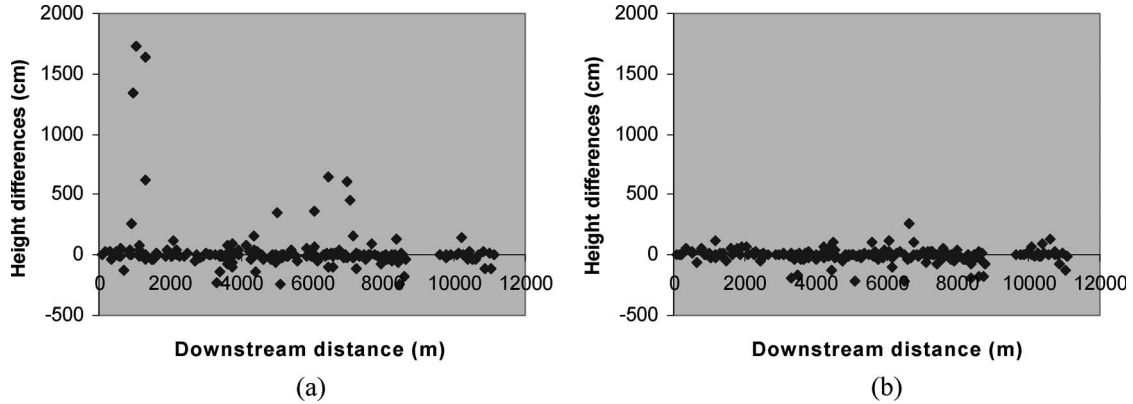
Fig. 8.   Paired height differences versus distance downstream for the parameter sets giving the minimum rms errors for the snake that was conditioned on (a) SAR data and (b) SAR and lidar data.

describe current performance measures based on binary patterns. One measure representative of these is

$$F^{(2)} = \left(A_{\mathrm{obs}} \bigcap A_{\mathrm{mod}} \right) \Big/ \left(A_{\mathrm{obs}} \bigcup A_{\mathrm{mod}} \right) \qquad (7)$$

where A_{obs} and A_{mod} represent the set of pixels that are observed to be inundated and predicted as inundated, respectively. $F^{(2)}$ is equal to 1 when observed and predicted areas coincide exactly and equal to 0 when no overlap between predicted and observed areas exists. A performance measure based on height differences might have several advantages over one such as $F^{(2)}$ based on binary pattern data. First, as the distribution of t is known, it is possible to estimate the probability $P(t > |t_0|)$ of obtaining a t value that is greater than the absolute value of that measured (t_0), whereas $F^{(2)}$ is simply a weight factor. Second, the height difference measure between two model runs with different parameter settings might turn out to be more sensitive than $F^{(2)}$, because a small change in mean height might cause a large change in $P(t > |t_0|)$ yet only a small change in $F^{(2)}$. Third, the sign of the t value identifies whether an overprediction or an underprediction has occurred, whereas $F^{(2)}$ may give similar values for overprediction and underprediction.

In this case, the parameters of the snake that was generated using SAR and lidar have been optimized using the aerial photo waterline, but this will not be available in the more usual situation in which the snake is being used to validate a model waterline. It is interesting that, for those nodes in areas of low slope and low vegetation, the standard deviation of their heights relative to their local mean height (within an 0.5-km distance) is a minimum at the same parameter setting at which the rms error of height differences between snake and aerial photo waterlines is minimized [Table I(b) and (c)]. This presumably reflects the fact that the snake is most smoothly varying when the relative height standard deviation is minimized, and it may be possible to use this measure as a surrogate for optimizing the snake parameters when using the snake to validate a modeled flood extent. However, a more likely scenario is that a single optimum parameter set would not be sought in this situation. In flood model validation, emphasis is now placed on associating uncertainties with model flood extents, by deriving flood extent

probability maps showing the probability of each pixel being flooded, given a flood event of the given magnitude. It has been found that, for a particular event, many different sets of model parameters may give flood extents that match the observed extent to a greater or lesser degree. Such equifinality has been well documented and has resulted in the development of the generalized likelihood uncertainty estimation (GLUE) technique, whereby many model runs are carried out, spanning the likely ranges of model parameters [35]. A flood extent probability map is obtained by performing a weighted average of the binary-valued modeled flood extents (with the value for a pixel being 1 for flooded and 0 for not flooded), with each model flood extent being weighted according to its performance measure relative to an observed flood extent. As previously mentioned, the performance measure could be based on patterns of height differences between observed and modeled waterlines rather than on patterns of wet or dry pixels. To date, the GLUE methodology has been mainly used to assess flood extent uncertainty due to model parameter errors (see, e.g., [21] and [36]). However, it seems a natural future step to try to extend the method to cope with uncertainty in both model and snake algorithm parameters [36]. Some method of limiting the number of model runs that are required would probably need to be employed (e.g., Gaussian emulation [37]), although some reduction might result from using an improved performance measure based on height differences.

VII. CONCLUSION

An algorithm has been developed for the automatic extraction of flood extent using a snake that was generated from combined SAR and lidar data, and the resulting waterline compared to that generated using SAR data alone. From the resulting snakes, sets of nodes in areas of low slope and low vegetation have been extracted, followed by further thinning. After optimization of parameters, the heights of the resulting node set from the snake that was conditioned on SAR and lidar matched the corresponding node heights from the aerial photo waterline significantly more closely than those from the snake that was conditioned solely on SAR data. The conclusion is that, for the variety of situations that are present in this particular

data set, the use of the lidar data has resulted in an observed waterline that varies more smoothly along the reach and is a better match to our best estimate of the true waterline heights.

ACKNOWLEDGMENT

REFERENCES

[1] P. D. Bates, M. S. Horritt, C. N. Smith, and D. C. Mason, "Integrating remote sensing observations of flood hydrology and hydraulic modeling," *Hydrol. Process.*, vol. 11, no. 14, pp. 1777–1795, 1997.
[2] L. C. Smith, "Satellite remote sensing of river inundation area, stage and discharge: A review," *Hydrol. Process.*, vol. 11, no. 10, pp. 1427–1439, 1997.
[3] F. T. Ulaby, R. K. Moore, and A. K. Fung, *Microwave Remote Sensing*, vol. 3. Norwood, MA: Artech House, 1986.
[4] J.-S. Lee and I. Jurkevich, "Coastline detection and tracing in SAR images," *IEEE Trans. Geosci. Remote Sens.*, vol. 28, no. 4, pp. 662–668, Jul. 1990.
[5] D. C. Mason and I. J. Davenport, "Accurate and efficient determination of the shoreline in ERS-1 SAR images," *IEEE Trans. Geosci. Remote Sens.*, vol. 34, no. 5, pp. 1243–1253, Sep. 1996.
[6] J. A. Richards, P. W. Woodgate, and A. K. Skidmore, "An explanation of enhanced radar backscattering from flooded forests," *Int. J. Remote Sens.*, vol. 8, no. 7, pp. 1093–1100, 1987.
[7] F. M. Henderson, "Environmental factors and the detection of open surface water using X-band radar imagery," *Int. J. Remote Sens.*, vol. 16, no. 13, pp. 2423–2437, 1995.
[8] S. I. Solomon, "Methodological considerations for the use of ERS-1 SAR imagery for the delineation of river networks in tropical forest areas," in *Proc. 1st ERS-1 Symp.*, Frascati, Italy, Jun. 26–27, 1995, pp. 595–600.
[9] M. S. Horritt, D. C. Mason, D. M. Cobby, I. J. Davenport, and P. D. Bates, "Waterline mapping in flooded vegetation from airborne SAR imagery," *Remote Sens. Environ.*, vol. 85, no. 3, pp. 271–281, May 2003.
[10] Y. Wang, L. L. Hess, S. Filoso, and J. M. Melack, "Understanding the radar backscattering from flooded and non-flooded Amazonian forests: Results from canopy backscatter modelling," *Remote Sens. Environ.*, vol. 54, no. 3, pp. 324–332, Dec. 1995.
[11] M. Badji and S. Dautrebande, "Characterisation of flood inundated areas and delineation of poor drainage soil using ERS-1 SAR imagery," *Hydrol. Process.*, vol. 11, no. 10, pp. 1441–1450, 1995.
[12] M. L. Imhoff, C. Vermillion, M. H. Story, A. M. Choudhury, A. Gafoor, and F. Poclyn, "Monsoon flood boundary delineation and damage assessment using space borne imaging radar and Landsat data," *Photogramm. Eng. Remote Sens.*, vol. 53, no. 4, pp. 405–413, 1987.
[13] H. Liu and K. C. Jezek, "Automated extraction of coastline from satellite imagery by integrating Canny edge detection and locally adaptive thresholding method," *Int. J. Remote Sens.*, vol. 25, no. 5, pp. 937–958, 2004.
[14] A. Niedermeier, E. Romaneessen, and S. Lehner, "Detection of coastlines in SAR images using wavelet methods," *IEEE Trans. Geosci. Remote Sens.*, vol. 38, no. 5, pp. 2270–2281, Sep. 2000.
[15] Y. Yu and S. T. Acton, "Automated delineation of coastline from polarimetric SAR imagery," *Int. J. Remote Sens.*, vol. 25, no. 17, pp. 3423–3438, Sep. 2004.
[16] P. A. Brivio, R. Colombo, M. Maggi, and R. Tomasoni, "Integration of remote sensing data and GIS for accurate mapping of flooded areas," *Int. J. Remote Sens.*, vol. 23, no. 3, pp. 429–441, Feb. 2002.
[17] G. Nico, M. Pappalepore, G. Pasquariello, A. Refice, and S. Samarelli, "Comparison of SAR amplitude vs. coherence flood detection methods—A GIS application," *Int. J. Remote Sens.*, vol. 21, no. 8, pp. 1619–1631, May 2000.
[18] M. S. Horritt, "A statistical active contour model for SAR image segmentation," *Image Vis. Comput.*, vol. 17, no. 3/4, pp. 213–224, Mar. 1999.
[19] M. S. Horritt, D. C. Mason, and A. J. Luckman, "Flood boundary delineation from synthetic aperture radar imagery using a statistical active contour model," *Int. J. Remote Sens.*, vol. 22, no. 13, pp. 2489–2507, Sep. 2001.
[20] G. Schumann, R. Hostache, C. Puech, L. Hoffmann, P. Matgen, F. Pappenberger, and L. Pfister, "High-resolution 3D flood information from radar imagery for flood hazard management," *IEEE Trans. Geosci. Remote Sens.*, vol. 45, no. 6, pp. 1715–1725, Jun. 2007.
[21] F. Pappenberger, K. Beven, M. Horritt, and S. Blazkova, "Uncertainty in the calibration of effective roughness parameters in HEC-RAS using inundation and downstream level observations," *J. Hydrol.*, vol. 302, no. 1–4, pp. 46–69, 2005.
[22] D. C. Mason, D. M. Cobby, M. S. Horritt, and P. D. Bates, "Floodplain friction parameterization in two-dimensional river flood models using vegetation heights derived from airborne scanning laser altimetry," *Hydrol. Process.*, vol. 17, no. 9, pp. 1711–1732, 2003.
[23] D. M. Cobby, D. C. Mason, M. S. Horritt, and P. D. Bates, "Two-dimensional hydraulic flood modelling using a finite element mesh decomposed according to vegetation and topographic features derived from airborne scanning laser altimetry," *Hydrol. Process.*, vol. 17, no. 10, pp. 1979–2000, 2003.
[24] G. Aronica, P. D. Bates, and M. S. Horritt, "Assessing the uncertainty in distributed model predictions using observed binary pattern information within GLUE," *Hydrol. Process.*, vol. 16, no. 10, pp. 2001–2016, 2002.
[25] D. S. Biggin and K. Blyth, "A comparison of ERS-1 satellite radar and aerial photography for river flood mapping," *J. Chart. Inst. Water Eng. Manag.*, vol. 10, pp. 1777–1795, 1996.
[26] L. M. G. Pereira and L. L. F. Janssen, "Suitability of laser data for DEM generation: A case study in the context of road planning and design," *ISPRS J. Photogramm. Remote Sens.*, vol. 54, no. 4, pp. 244–253, 1999.
[27] I. J. Davenport, N. Holden, and R. J. Gurney, "Characterizing errors in airborne laser altimetry data to extract soil roughness," *IEEE Trans. Geosci. Remote Sens.*, vol. 42, no. 10, pp. 2130–2141, Oct. 2004.
[28] D. J. Williams and M. Shah, "A fast algorithm for active contours and curvature estimation," *CVGIP, Image Underst.*, vol. 55, no. 1, pp. 14–26, Jan. 1992.
[29] J. Ivins and J. Porrill, "Statistical snakes: Active region models," in *Proc. 5th Brit. Mach. Vis. Conf.*, York, U.K., Sep. 1994, vol. 1 and 2, pp. 377–386.
[30] M. S. Horritt, "Psnake NT user manual," Univ. Bristol, Bristol, U.K., 2002. School of Geographical Sciences Report.
[31] D. C. Mason, T. R. Scott, and H.-J. Wang, "Extraction of tidal channel networks from airborne lidar data," *ISPRS J. Photogramm. Remote Sens.*, vol. 61, no. 2, pp. 67–83, 2006.
[32] C. V. Deutsch and A. Journel, *GSLIB: Geostatistical Software Library and Users's Guide.* New York: Oxford Univ. Press, 1992, p. 41.
[33] P. D. Bates, M. Wilson, M. S. Horritt, D. C. Mason, N. Holden, and A. Currie, "Reach scale floodplain inundation dynamics observed using airborne SAR imagery," *J. Hydrol.*, vol. 328, no. 1/2, pp. 306–318, 2006.
[34] S. Neelz, G. Pender, I. Villanueva, M. D. Wilson, N. G. Wright, P. D. Bates, D. C. Mason, and C. Witlow, "Using remotely sensed data to support flood modelling," *Proc. Inst. Civil Eng.*, vol. 159, no. 1, pp. 35–44, 2006.
[35] K. J. Beven and A. M. Binley, "The future of distributed models: Model calibration and predictive uncertainty," *Hydrol. Process.*, vol. 6, no. 3, pp. 279–298, 1992.
[36] M. S. Horritt, "A methodology for the validation of uncertain flood inundation models," *J. Hydrol.*, vol. 326, no. 1–4, pp. 153–165, 2006.
[37] J. E. Oakley and A. O'Hagan, "Probabilistic sensitivity analysis of complex models: A Bayesian approach," *J. R. Stat. Soc., Series B*, vol. 66, no. 3, pp. 751–769, Aug. 2004.

David C. Mason received the B.Sc. and Ph.D. degrees in physics from the University of London, London, U.K., in 1963 and 1968, respectively.

He was with the U.K. Medical Research Council and Plessey Electronic Systems Research. Since 1984, he has been with the Natural Environment Research Council Environmental Systems Science Centre, University of Reading, Reading, U.K., carrying out research on the automated extraction of information from remotely sensed data and linking these data to environmental models. His current research interests include using remotely sensed data for validation and parameterization of river flood models and assimilation into coastal morphodynamic models.

Matthew S. Horritt received the Ph.D. degree from the University of Reading, Reading, U.K., in 1998.

He was with the University of Leeds, Leeds, U.K., and the Department of Civil Engineering, University of Bristol, Bristol, U.K., as a Postdoctoral Research Fellow and a Lecturer in civil engineering, respectively. He is currently a Specialist Modeler with Halcrow Group Ltd., London, U.K. His research interests are flood inundation models, remote sensing of floods and floodplain topography, and model validation.

Johanna T. Dall'Amico is currently working toward the B.Sc. degree in mathematics at the University of Reading, Reading, U.K., and a Diploma in geography and remote sensing at Ludwig-Maximilian University of Munich, Munich, Germany.

She is a Visiting Student at the Natural Environment Research Council Environmental Systems Science Centre, University of Reading, where she works on remote sensing applications for fluvial flood models.

Tania R. Scott received the B.Sc. degree in astronomy from the University of Canterbury, Christchurch, New Zealand, in 1992 and the Ph.D. degree in astronomy from the University of Cambridge, Cambridge, U.K., in 1998.

She was with the U.K. Met Office, where she developed meteorological products for the aviation industry to address safety and environmental issues. She is currently with the Natural Environment Research Council (NERC) Environmental Systems Science Centre, University of Reading, Reading, U.K., where she is interested in using remote sensing data in aid of environmental modeling. Her current project is to apply data assimilation techniques to coastal area morphodynamic modeling, which is funded under the NERC program Flood Risk from Extreme Events.

Paul D. Bates received the Ph.D. degree from the University of Bristol, Bristol, U.K., in 1993, with support from a Natural Environmental Research Council studentship.

Subsequently, he has been with at the University of Bristol as a Postdoctoral Researcher and Lecturer, and has been a Full Professor since 2003. He is currently the Director of the Hydrology Research Group, School of Geographical Sciences, University of Bristol. He has been a Visiting Scientist at Princeton University, Laboratoire National D'Hydraulique, Paris, and the EU Joint Research Centre, Ispra, Italy. His research interests include the development and analysis of numerical models for predicting river flood flows, principally using data derived from remote sensing sources, spatial prediction, risk, and uncertainty. He is the Editor-in-Chief of the *International Journal of River Basin Management*.